Two-Stage Microgrid Resilience and Battery Life-Aware Planning and Operation for Cyclone Prone Areas in India

Abstract

Microgrid (MG) resilience is crucial for modern power systems, due to the rising threats from High-Impact Low-Probability (HILP) events, such as natural disasters and cyberattacks. Effective management of microgrid resiliency has become a critical research area, yet operational resiliency studies often overlook microgrid sizing or rely on generic designs rather than actual resource and load data, and rarely incorporate real extreme weather events for performance validation. This paper proposes a two-stage approach for optimal design and resilient operation of the microgrid system. In the first stage, the microgrid's photovoltaic (PV) arrays, wind turbines (WT), converters, and battery units are sized using HOMER Pro for a coastal village near Ongole, India, based on realistic solar and wind data. In the second stage, a model predictive control-based Mixed Integer Linear Programming (MILP) model with load shifting demand response optimizes real-time operation. An expected resiliency index enables smart control by dynamically adjusting objective function weights and battery state of charge limits, while a novel battery life cycle–depth of discharge formulation enhances battery life expectation. Resiliency is assessed using historical solar and wind data from Cyclone Laila. Simulation results indicate that a 140-kW PV, 80-kW WT, 52-kW converter, and 780 kWh lithium-ion battery system can meet the village's load demand in both grid-connected and islanded modes during the HILP event. In grid-connected mode, excess energy sales reduce the Cost of Energy to \$0.163/kWh, compared to \$0.237/kWh in islanded mode. Under resilient operation with demand response, the system delivers an expected battery life of 15.5 years and approaches a resiliency index of close to 1.0. Grid connection doubles battery life while ensuring full load supply during HILP events. Even with reduced planned battery capacity scenarios, the proposed control maintains robust resiliency. These findings indicate that the proposed two-stage framework provides a scalable and sustainable strategy for enhancing MG resilience and battery longevity in regions prone to extreme weather events.

Keywords: Microgrid Sizing, Power System Resiliency and Reliability, Model Predictive Control, Smart Grids

Nomenclature

AMI	Advanced Metering Infrastructure
BESS	Battery Energy Storage System
BLC	Battery Life Cycle
BM	Bio-Mass
CG	Conventional Generation
CHP	Combined Heat and Power
COE	Cost Of Energy
DE	Differential Evolution
DERs	Distributed Energy Resources
DG	Distributed Generation
DiG	Diesel Generator
DOD	Depth Of Discharge
DRL	Deep Reinforcement Learning
ERC	Expected Resiliency Curve
ERI	Expected Resiliency Index
EV	Electric Vehicle
EY	Expected Years
FC	Fuel Cells
GHI	Global Horizontal Irradiance
GT	Gas Turbines
HILP	High Impact Low Probability
HP	Hydro Power
IOI	Independent Operation Index
IWOA	Improved Whale Optimization Algorithm
LF	Load-Following
MDP	Markov Decision Process
MILP	Mixed-Integer Linear Programming
MINLP	Mixed-Integer Non-Linear Programming
MIQP	Mixed-Integer Quadratic Programming
MPC	Model Predictive Control
MT	Micro Turbines
NLP	Non-Linear Programming
NOCT	Nominal Operating Cell Temperature
NREL	National Renewable Energy Laboratory
NSGA-II	Non-dominated Sorting Genetic Algorithm
NYISO	New York Independent System Operator
O&M	Operation and Maintenance
POA	Plane of Array
POWER	Prediction of Worldwide Energy Resources
PV	Photo Voltaic
RES	Renewable Energy Resources
RI	Resilient Index
RTE	Round-Trip Efficiency
SAURN	Southern African Universities Radiometric Network
SOC	State of Charge
SOH	State Of Health
SSA	Salp Swarm Algorithm
STP	Standard temperature and Pressure
TNPC	Total Net Present Cost
TS	Total Switches
WT	Wind Turbine
WTG	Wind Turbine Generator

1. Introduction

Modern power systems are recognized for their reliability, yet they face increasing challenges due to the rise in High-Impact, Low-Probability (HILP) events, such as natural disasters like typhoons and cyclones, as well as human-induced incidents like cyberattacks. These challenges have brought greater attention to resiliency studies in power systems. The focus of these studies is to ensure that during HILP events, critical power loads are prioritized first, followed by the restoration of all other loads [1].

Simultaneously, the development of smart grids has introduced new dynamics into the power sector. Enabled by Advanced Metering Infrastructures (AMIs), which allow for bidirectional communication within power systems, smart grids have given rise to areas of research such as microgrids, demand-side management, prosumers, and self-healing networks [2]. The global push towards renewable energy, driven by concerns about climate change, adds another layer of complexity. While renewable energy sources offer environmental benefits, they are considered intermittent production systems. To address the reliability issues associated with renewable energy, microgrids often

incorporate Battery Energy Storage Systems (BESSs). Given that BESSs constitute a significant portion of microgrid costs, their longevity is a critical factor in ensuring the sustained operation of these systems.

Microgrids, which can function in both isolated and grid-connected modes, are particularly effective in harnessing renewable energy. In remote areas where connecting to the main grid is either impractical or uneconomical, electrification can be achieved through clean energy production using isolated microgrids. The planning and sizing of microgrids in such regions depend heavily on local weather conditions and load characteristics. Additionally, it is essential to evaluate the design from an operational perspective after the planning phase. In addition to standalone microgrids, interconnected multi-microgrid (mMG) systems offer potential cost reductions and resilience improvements through energy sharing [3].

The following section presents a comparative literature review of the various contributions made by other researchers on planning, operation, and multi-stage processes of microgrid design, including battery longevity. This review aims to identify research gaps and highlight the contributions of this work.

1.1. Literature Review and Research Gaps

The exploration of microgrid design and operation has become increasingly crucial as modern power systems adapt to evolving challenges. While extensive research has focused on microgrid planning and sizing, few directly evaluate real-world operational performance under severe conditions or with empirical data.

Various studies have proposed frameworks for integrating renewable energy sources and optimizing their placement in the planning stage. For instance, [4] introduces a data-driven framework that deploys wind turbines (WT), photovoltaics (PV), and microturbines (MT) into existing networks while accounting for uncertainties in renewable generation through historical weather data. The framework was tested on an IEEE 33-bus system, using weather data from the Southern African Universities Radiometric Network (SAURN) and load data from the New York Independent System Operator (NYISO). However, data sources are synthetic for this study. In parallel, [5] uses a multi-agent Deep Reinforcement Learning (DRL) approach with a multi-objective Mixed-Integer Non-Linear Programming (MINLP) to allocate Renewable Energy Resources (RES), BESS, and Electric Vehicle (EV) charging. The framework considers power loss, capital and operational costs, environmental impact, and system voltage stability. Practical distribution networks in Bangladesh and Turkey are considered for the case study. Other contributions focus on enhancing network resilience: [6] identifies the optimal nodes for microgrid components within a distribution network, and [7] proposes clustering active distribution networks into multiple MGs while emphasizing performance indices such as the Independent Operation Index (IOI) and Round-Trip Efficiency (RTE). Although the weather data used is specific to a location in Malaysia, the network model is the standard IEEE-33 bus system. A long-term expansion planning approach for microgrids, designed to serve as backup power systems during outages, is proposed in [8]. This problem

is formulated as a Markov Decision Process (MDP) and solved using DRL, with an emphasis on system resiliency. In line with techno-economic analyses, [9] evaluates both isolated and grid-connected microgrids in Putrajaya City, Malaysia, using HOMER Pro to identify a cost-effective mix of WT, PV, BESS, and Bio-Mass (BM). Yet, the study does not extend to operational performance under HILP events. A similar emphasis on economic feasibility is found in [10], which employs Differential Evolution (DE) to design a standalone microgrid for rural electrification in India, but likewise does not investigate resilience under actual disruptive conditions. Although various works [4, 5, 9, 10] suggest methods for microgrid sizing, few systematically re-evaluate that sizing or examine performance under real-world operational conditions, particularly during extreme events.

Multi-stage frameworks have emerged as a promising strategy to handle uncertainties and improve microgrid resiliency through sequential decision-making. For instance, [11] introduces a two-stage stochastic model for multi-microgrid planning in which the first stage addresses uncertainties using Non-Linear Programming (NLP), and the second focuses on both long-term purchasing and short-term operational constraints; however, aspects such as resiliency, smart grid technologies like demand response, and battery life considerations in operation are neglected. Additionally, the study realistically estimates the rooftop solar limits in the state of São Paulo, Brazil. Similarly, [12] explores a two-stage solution targeting planned n-1 outage of diesel generators and real-time microgrid operation under uncertainties in Canada. In another two-stage setting, [13] applies Mixed-Integer Linear Programming (MILP) to schedule various renewable sources, dividing the process into day-ahead generation planning and intra-day adjustment with waste conversion systems and incentive-based demand response. A more resilience-focused two-stage framework is introduced by [14], which formulates a microgrid formation strategy for enhancing distribution network resilience against earthquakes. The first stage models an earthquake event using geographical data, peak ground acceleration, and fragility curves, while the second stage applies graph theory and linear programming to form microgrids and optimize operational states. Beyond two-stage paradigms, [15] advances a three-level resilience-centric approach for multi-microgrids, using an Adaptive Genetic Algorithm (AGA) to model potential attacks and the Non-dominated Sorting Genetic Algorithm (NSGA-II) to balance cost and resiliency. The study identified that improving resiliency increases costs in general, but employing multi-microgrid systems reduces investment compared to standalone microgrids. Finally, [16] proposes a three-stage framework addressing network reinforcement by line hardening and Distributed Generation (DG) placement, microgrid formation upon grid disconnection, and demand-side management to reduce load shedding and costs. Multi-carrier energy microgrids (MCEMs) also offer a pathway to integrate diverse energy carriers and enhance resilience via cooperative methods. For example, [3] employs game-theoretic tools (Shapley value, nucleolus) in a cost-aware optimization model, demonstrating that coalition-based energy management lowers lifecycle and operational costs without compromising outage resilience. Likewise, [17] uses a tri-level,

two-stage stochastic framework to enable energy trading between distribution networks and MCEMs, achieving a 2.7% reduction in planning costs and highlighting the value of resilience in high-level investment decisions. Heuristic methods also feature prominently in microgrid research, typically aiming to minimize costs or emissions under various uncertainties. For example, [18] proposes an optimization approach using the heuristic Salp Swarm Algorithm (SSA) to reduce both operational costs and pollution across multiple energy sources (WT, PV, BESS, MT, DiG, and Fuel Cells (FC)). Although this approach incorporates uncertainty modeling for electricity pricing, load consumption, and renewable generation, it limits battery operation to simple charge–discharge modes and provides limited information about the specific microgrid location. In a related study, [19] leverages the CSAJAYA heuristic algorithm to design a demand response program for a grid-connected microgrid containing Gas Turbines (GT), FC, and Conventional Generation (CG), with an emphasis on reducing emissions and costs. Meanwhile, [20] proposes an operational planning approach for a grid-connected microgrid using the meta-heuristic Improved Whale Optimization Algorithm (IWOA) and compare its performance with other heuristic methods. Beyond metaheuristic techniques, uncertainty-driven approaches have also been explored to enhance microgrid resilience operation. For instance, [21] introduces a hybrid probabilistic-possibilistic self-scheduling framework that incorporates CVaR to manage financial risks associated with HILP events. This study focuses on improving decision-making under uncertainty by integrating stochastic electricity prices, wind power fluctuations, reserved deployment, forced outage rates, and HILP event into a comprehensive scheduling model. Many existing studies [5, 18, 6, 7, 4, 22, 23, 24, 25] rely on idealized or test-case data rather than authentic, location-specific measurements, which can obscure potential vulnerabilities in the face of HILP events.

Recent research has also emphasized battery lifespan, although most approaches do not fully capture the complexity of Depth Of Discharge (DOD) impacts. Like many studies that consider battery longevity through simple SOC constraints, [26] and [27] focus on limiting SOC to improve efficiency and reduce degradation in transportable storage systems and shared BESS, respectively. Beyond SOC control, [28] applies an EV charge-discharge scheduling model to restrict cycling and minimize battery deterioration, while [29] adopts a simplified linear capacity degradation model that overlooks nonlinear aging effects. In [22], a microgrid operation model incorporating PV systems, WT, and BESS is proposed. The study aims to minimize switching costs by introducing a battery idle mode. However, this approach does not necessarily enhance battery longevity, as battery life is more dependent on the DOD rather than the number of switches. Improved battery life is shown as a by-product of their optimization rather than being a primary objective. Building on the previous work mentioned earlier, [23] enhances the model by addressing the battery life cycle in optimization problems and proposing a Model Predictive Control (MPC) model for the resilient operation of isolated microgrids. However, this study still overlooks important aspects such as microgrid sizing and the real-world scenario of an HILP event. A distributed MPC approach for the operation of multi-microgrids, considering the State Of Health

(SOH) of the battery, is proposed by [24]. The study addresses cycle aging using a simplified linear equation related to battery discharge, though the relationship between these factors is more complex and not strictly linear. In [30] and [25], the authors employ a stepwise linearization approach to model battery cycle aging, discretizing the DOD into predefined intervals and assigning constant cycle life values within each range. While these methods offer a simplified representation of battery degradation, they introduce abrupt discontinuities that do not accurately reflect the gradual nature of battery aging. In contrast, the present study treats the Battery Life Cycle–Depth of Discharge (BLC–DOD) curve as piecewise linear. This guarantees a smoother transition between DOD levels and improves model accuracy and implementation ease. This approach not only improves battery operation modelling but also bridges gaps in microgrid sizing and resilience, providing a more robust framework for optimizing battery performance in real-world applications. Most battery-aging models [26, 27, 28, 29, 22, 24] either neglect DOD considerations or use oversimplified parameters (e.g., bounding state of charge) rather than a detailed approach. Also, resiliency often appears as a byproduct of broader operational strategies instead of being explicitly integrated into the objective function in the reviewed articles.

Studies combining microgrid design and subsequent operational analysis offer a closer approximation to practical implementations. An interesting work by [31] employs a two-stage framework for the design and sizing of a microgrid in Kangaroo Island using HOMER Pro, followed by the performance evaluation of the best-designed microgrid with MATLAB/Simulink and DIgSILENT software. The study assesses the system's performance based on reliability indices, voltage and frequency stability, and real and reactive power analysis. Likewise, a framework for determining the optimal sizing of rural isolated microgrids using improved MILP is proposed in [32]. The system is then evaluated using different control approaches in MATLAB, focusing on power quality, total harmonic distortion, and voltage regulation.

To summarize the research gaps and novel contributions, Table 1 shows a comparative summary of the ongoing literature across various aspects. These aspects include planning and operation modes, renewable technologies used, microgrid configurations (isolated or grid-connected), demand response, resiliency, battery life considerations, software employed, and real-case scenario analysis.

1.2. Contributions

To address the gaps mentioned in section 1.1, this work presents a two-stage framework that incorporates real data for microgrid sizing and HILP event analysis, models battery longevity, and integrates resiliency directly into operations. The main contributions are:

1. A microgrid was planned for a village in Andhra Pradesh, India, using HOMER Pro with real load data. The

Table 1: Comparative analysis of microgrid design and operational literature.

Ref	Technology	Mode	DR	Resiliency	Battery Life	Software	Real Case	Planning (P) Operation (O)
[4]	WT-PV-MT	IS/GC	-	-	-	CPLEX(MILP)	-	P
[22]	WT-PV-BESS	IS	-	-	✓	MATLAB(YALMIP)	-	O
[18]	WT-PV-BESS-MT-DiG-FC	IS/GC	-	-	-	MATLAB(SSA)	-	O
[15]	ESS	IS	-	✓	-	IPOPT(AGA)	-	P
[6]	WT-PV-ESS	GC	-	✓	-	MATLAB-CPLEX	-	P
[7]	WT-PV-BESS	IS	-	-	-	MATLAB	-	P
[19]	WT-PV-GT-FC-CG	IS/GC	✓	-	-	MATLAB(CSAJAYA)	-	O
[20]	WT-PV-BESS-DiG-FC	GC	-	-	-	-(IWOA)	-	O
[16]	DG	IS	✓	✓	-	GAMS(CPLEX)	-	P
[25]	WT-PV-DG	GC	-	-	✓	CPLEX(MILP)	-	P
[24]	WT-PV-BESS	IS	✓	-	✓	MATLAB-GAMS	-	O
[23]	WT-PV-BESS	IS	-	✓	✓	Pyomo (MILP)	-	O
[11]	PV-BESS	GC	-	-	-	GAMS(NLP/MILP)	✓	P
[9]	WT-PV-BESS-BM	IS/GC	-	-	-	HOMER Pro	✓	P
[5]	WT-PV-BESS-EV	GC	-	-	-	-(MINLP)	✓	P
[12]	WT-BESS-DiG	GC	-	-	-	MATLAB(Heuristic)	✓	O
[10]	WT-PV-BESS-DiG	IS	-	-	-	MATLAB(DE)	✓	P
[13]	WT-PV-BM-EV-HP	GC	✓	-	-	-(MILP)	✓	O
[31]	WT-PV-BESS-DiG	IS	-	-	-	HOMER Pro DIgSILENT	✓	P/O
[32]	WT-PV-BSS-BM	IS	-	-	-	MATLAB-MILP	✓	P/O
[8]	WT-PV-ESS-DiG-HP-CHP	IS	-	✓	-	-(DRL)	✓	P
Current Work	WT-PV-BESS	IS/GC	✓	✓	✓	HOMER Pro Pyomo (MILP)	✓	P/O

Note: WT: Wind Turbine, PV: Photovoltaic, BESS: Battery Energy Storage System, MT: Microturbine, DiG: Diesel Generator, FC: Fuel Cell, ESS: Energy Storage System, DG: Distributed Generation, GT: Gas Turbine, CG: Conventional Generation, BM: Bio-Mass, EV: Electric Vehicle, HP: Hydro Power, CHP: Combined Heat and Power, DR: Demand Response, IS: Islanded Mode, GC: Grid-Connected Mode, MILP: Mixed-Integer Linear Programming, NLP: Non-Linear Programming, MINLP: Mixed-Integer Nonlinear Programming, SSA: Salp Swarm Algorithm, AGA: Adaptive Genetic Algorithm, IWOA: Improved Whale Optimization Algorithm, DRL: Deep Reinforcement Learning, DE: Differential Evolution.

design was then validated under the actual HILP event of Cyclone Laila by remodelling all components within a MILP framework.

2. The microgrid energy management objective function integrates the Battery Life Cycle–Depth of Discharge (BLC–DOD) relationship. In addition, a piece-wise linear approximation of the BLC–DOD curve enables near optimal solution from the MILP formulation. This explicit consideration of battery aging refines operational decisions on charging, discharging, and idle modes.
3. For the resiliency aspect, the Expected Resiliency Curve (ERC) was introduced within an MPC framework. Additionally, by minimizing the area under the power imbalance curve, the system's resiliency was enhanced. This involved mathematical manipulation of formulas to incorporate resiliency into the objective function directly.

1.3. Paper Organization

This section has identified the research gaps and outlined the contributions of this article. Section 2 will present the proposed two-stage framework, followed by a detailed model and formulation of both the planning and operation stages, along with the input data. Section 3 will first discuss the results obtained from the planning stage and then evaluate the performance of the optimally sized microgrid during a HILP event as a worst-case scenario. The final

section will discuss the findings, present conclusions, and propose future research directions.

2. Micro-grid Model

The microgrid in this study consists of three main loads with different priorities: essential, business, and deferred load. The load data considering the electricity demand for domestic use, agricultural, community, small-scale industrial and for rural commercial activities is estimated for a coastal village near Ongole in Andhra Pradesh (India), which has been impacted by cyclones over the past decades. The proposed microgrid relies entirely on renewable energy sources, including wind turbines and PV modules, supported by a BESS and a converter to ensure reliable power generation. Real weather data from the SARAH satellite, available on the PVGIS website, was used, specifically focusing on the conditions during Cyclone Laila in mid-May 2010 [33, 34]. [1]

In this article, a two-stage model is introduced. In the first stage, a general microgrid is designed to meet load demands under normal conditions using HOMER Pro, as shown in Figure 1a. In this Figure, the term LI ASM refers to the Lithium-Ion Advanced Statistical Model, which is utilized to simulate the performance of lithium-ion batteries within the microgrid design, allowing for a more accurate assessment of their behaviour under varying operational conditions. After determining the nominal ratings of the microgrid components, the entire system is modeled as a MILP problem (see Figure 1b). A sliding window MPC approach is then applied to evaluate its performance under the HILP event, with a more detailed discussion provided in the section 2.2.1. In Section 2.1, the planning model and parameters will be discussed in more detail, while Section 2.2 provides an in-depth look at the operational aspects.

The framework can easily be adapted to different regions with varying weather and regulations. In the planning phase, HOMER Pro allows customization of local solar and wind data, as well as regulatory factors. This makes the framework suitable for different locations. In the operational phase, the MILP–MPC strategy remains effective. It can adjust to various weather patterns and regulations, ensuring that the model optimizes battery use and demand response in areas with more frequent, but less extreme, weather disruptions.

2.1. Micro-grid Planning Stage Model

A microgrid consists of Distributed Energy Resources (DERs) such as photovoltaic systems, bi-directional inverters with energy storage devices and load demands, which are situated closer to the customer and perform as a single well-regulated unit with reverence to the grid. The modelling of the different components of the microgrid system is presented in 2.1.2.

[1] For further details, see `https://re.jrc.ec.europa.eu/pvg_tools/en/`.

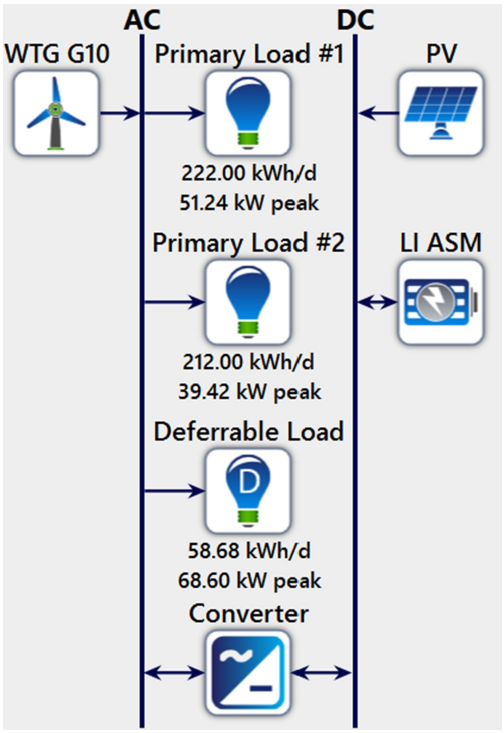

(a)

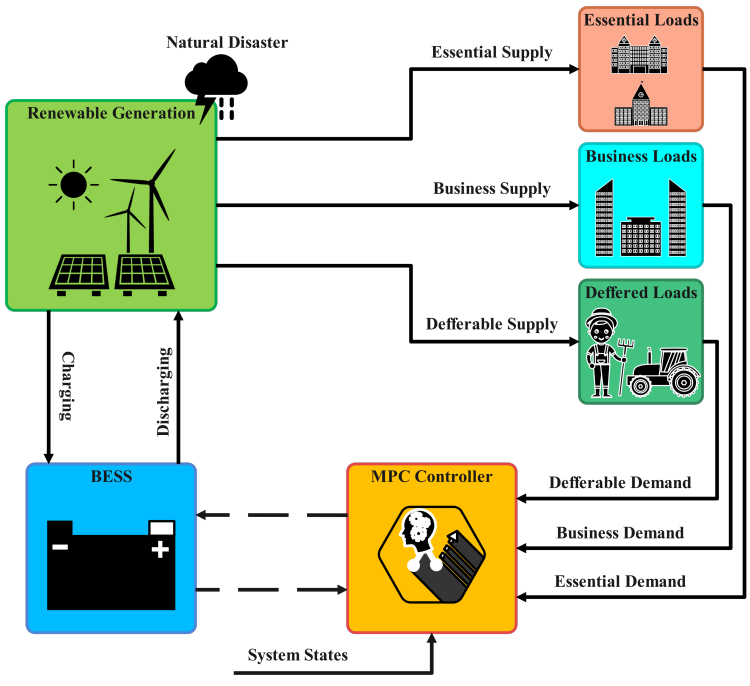

(b)

Figure 1: Two-stage microgrid design and operation model: (a) Homear based Microgrid Planning Model, (b) Microgrid Operation Model.

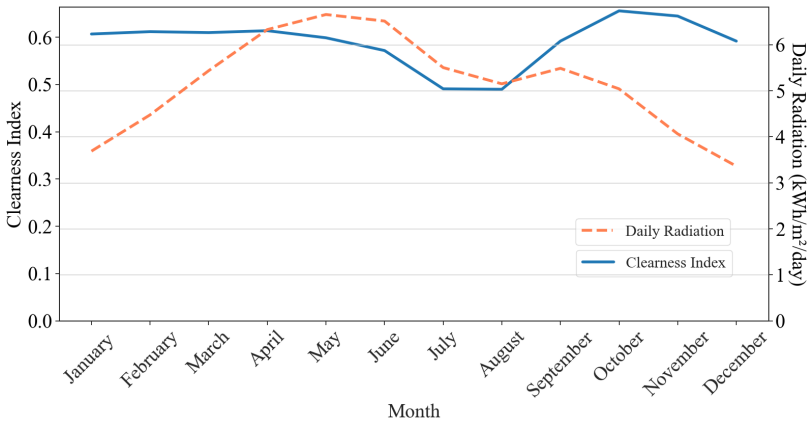

(a)

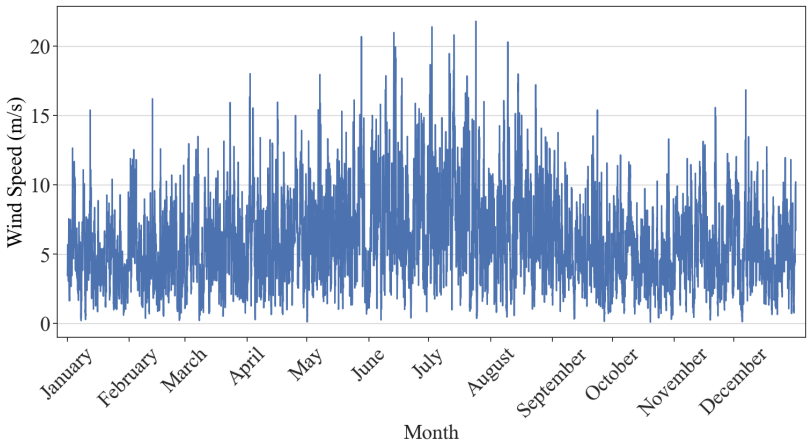

(b)

Figure 2: Annual data: (a) Solar GHI (Global Horizontal Irradiance), (b) Wind speed at the selected location.

2.1.1. Estimated load profile and resource data at the selected location

Weather Data: Figure 2a and 2b present the annual data for solar Global Horizontal Irradiance (GHI) and wind speed, respectively. The solar GHI data was sourced from the National Renewable Energy Laboratory (NREL) database while the wind speed data was obtained from NASA's Prediction of Worldwide Energy Resources (POWER) database corresponding to a location in Kottapatnam, a small coastal village situated in the Ongole revenue division of the Prakasam district in the Indian state of Andhra Pradesh. The geographical coordinates of this location are 15°28′36.3"N latitude and 80°11′54.0"E longitude.

Load Data: The electricity demand is lower in rural areas compared to urban areas. In most of the remote rural villages, the main load comprises domestic (e.g., radios, lamps, fans), agriculture (e.g., water pumping), community services (e.g., schools, clinics), and small-scale commercial activities (e.g., cold storage, milk processing) loads. The village's energy needs are accounted for according to seasonal variations: summer (April to October) and winter (November to March) and the load demand is categorized into three main types as follows [35]:

1. Primary Load-1 (Essential Loads): It includes domestic use appliances load (lamps, fans, radio), medical centres, and schools, with a daily demand of 222 kWh with a peak of 51.2 kW, and a load factor of 0.181.
2. Primary Load-2 (Business Loads): It includes community centres, local businesses, and small manufacturers, street light load with a daily demand of 212 kWh with a peak of 39.4 kW, and a load factor of 0.224.
3. Deferred Load (Agricultural Loads): This type of load mainly contains agricultural irrigation pump load with a daily average of 58.6 kWh and a peak load of 68.6 kW, having a storage capacity of 30 kW.

The complete details of the number and types of loads, wattage of the various appliances, and their 24-hour load utilization pattern are provided in [36]. Figure 3 shows the average hourly load data in the planning stage, separating essential and business loads to illustrate demand variations throughout the day.

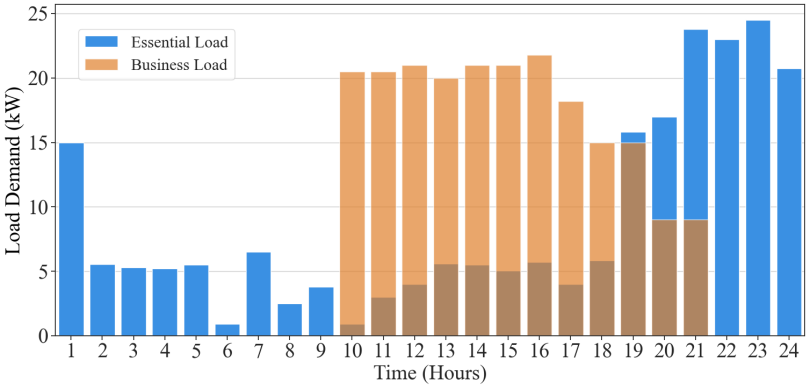

Figure 3: Average hourly load profile for essential and business loads in the planning stage.

2.1.2. Mathematical Representation

Solar Photovoltaic Generation: The power generated (P_{PV}) by solar PV generating system can be calculated as follows:

$$P_{PV} = C_{PV} D_{PV} \left[\frac{I_T}{I_T^{\text{STC}}}\right] \left[1 + \alpha_P \left(T_C - T_C^{\text{STC}}\right)\right], \tag{1}$$

where C_{PV} is the rated capacity of PV in kW and the derating factor of the PV array is represented by D_{PV}. Solar radiation incidents in kW/m^2 on the PV array and at standard test conditions are represented by I_T and I_T^{STC}, respectively. The temperature coefficient of power in percentage per degree Celsius (%/°C), is denoted by α_P. T_C and T_C^{STC} is cell temperature in °C and cell temperature at standard test conditions, respectively.

The energy balance for PV module is:

$$\tau_\alpha = \frac{I_T \eta_{PV} + U_L \times (T_C - T_a)}{I_T}, \tag{2}$$

where τ_α denotes the fraction of incident sunlight that is either absorbed or transmitted through the panel, which is known as absorptance-transmittance. The PV array efficiency and the heat transfer coefficient from the surroundings are denoted by η_{PV} and U_L, respectively. In addition, the cell and ambient temperature are symbolised by T_C and T_a, respectively [37].

As per the manufacturer's specification, the value of τ_α used in Equation 2 can be calculated at the Nominal Operating Cell Temperature (NOCT) with other conditions. The value of τ_α can vary due to the manufacturer's specification and calculated at NOCT after considering the other parameters values such as at 20°C ambient temperature, $0.8/kW/m^2$ of solar irradiation, and at no load conditions (i.e. $\eta_{PV} = 0$) [38, 39]. Rearranging Equation 2 leads to:

$$\tau_\alpha = U_L \times \frac{T_C^{\text{NOCT}} - T_a^{\text{NOCT}}}{I_T^{\text{NOCT}}}, \tag{3}$$

where, irradiation of the solar at NOCT ($0.8/kW/m^2$), the NOCT, and the atmospheric temperature at NOCT are denoted by I_T^{NOCT}, T_C^{NOCT} and T_a^{NOCT}.

HOMER takes the value of τ_α as 0.9. By utilizing the value of τ_α, the cell temperature of the PV panel can be calculated and expressed as follows [37]:

$$T_C = T_a + I_T \left(\frac{T_C^{\text{NOCT}} - T_a^{\text{NOCT}}}{I_T^{\text{NOCT}}} \right) \left(\frac{1 - \eta_{PV}}{\tau_\alpha} \right). \tag{4}$$

The multi-crystalline PV panels (Generic Flat plate) with an efficiency of 14.5% are considered in the proposed microgrid system [40]. The derating factor which takes into account various factors such as dust particles, snow cover, high temperature, aging, and wiring losses is considered as 80% and 20 years is the lifetime of the PV panels [41]. The capital cost of the PV system is considered as 741 \$/kW, while the replacement cost, operation cost, and maintenance cost of the PV system taken under consideration taken as 741 \$/kW and 25 \$/kW/year, respectively [40, 42]. The capital cost comprises expenses related to delivery, installation, and the necessary wiring and mounting hardware.

Wind Turbine Generator (WTG): The power output of the WTG can be determined using the following equation:

$$P_{\text{WT}}(v) = \begin{cases} \frac{P_{WT}^{rat}(v - v^{\text{cin}})}{v^{\text{rat}} - v^{\text{cin}}} & \text{if } v^{\text{cin}} \le v \le v^{\text{rat}} \\ P_{WT}^{rat} & \text{if } v^{\text{rat}} \le v \le v^{\text{co}} \\ 0 & \text{if } v \le v^{\text{cin}} \text{ or } v \ge v^{\text{co}} \end{cases}, \tag{5}$$

where P_{WT}^{rat} represents the power rating of a single WTG, v^{cin} and v^{CO} denote the cut-in and cut-out wind speeds, respectively, v stands for the wind speed at the desired height, and v^{rat} is the rated wind speed [37].

The speed of the wind mainly depends on the geographic location and hub height of the wind turbine and mathe-

matically it can be represented using the following equations:

$$v = v^{ref}\left(\frac{H}{H^{ref}}\right)^{\alpha}, \tag{6}$$

where the wind velocity at the height of 'H' is represented by v whereas the wind velocity calculated at the reference height (H^{ref}) is designated by v^{ref}. Additionally, the exponent α is influenced by factors such as wind speed, surface roughness, time of day, temperature, and season. Its value ranges from 0.4 for rough surface conditions in temperate latitudes to 0.05 for smooth surface conditions in tropical regions [37]. The value of α is 0.142 according to consistent wind flow in the selected location in this study for the planning stage. The variation in air density can also affect the actual power output of the WTG. HOMER adjusts the power value, obtained from the power curve, by multiplying it with the air density ratio to account for real-world conditions. Overall, mathematically it can be represented by the following equation:

$$P_{WT} = \left(\frac{\rho}{\rho_0}\right) P_{WT}^{STP}, \tag{7}$$

where P_{WT}^{STP} denotes the WTG power output at Standard Temperature and Pressure (STP), ρ is the actual air density, ρ_0 is the air density at STP (1.225 kg/m^3) [37, 39].

A generic WT based generator of 10 kW rating capacity having the capital cost, replacement cost, and O&M of $11539, $11539, and 230 $/year, respectively have been considered during the simulation [39, 35]. The lifetime and the hub height of the WT based generator are considered 20 years and 50 m, respectively [35]. The cut-in speed (v^{cin}), cut-out speed (v^{co}) and rated wind speed (v^{rat}) of 10 kW WTG are taken as 3 m/s, 25 m/s and 12 m/s, respectively [35]. The capital cost of the generator includes expenses for the tower, turbine, rotor, control system, wiring, and installation.

Converter: The power rating of a bidirectional converter interfacing AC and DC buses can be calculated using the following formula [41]:

$$P_{\text{con}} = \frac{P_L}{\eta_{\text{con}}}, \tag{8}$$

where, P_L and η_{con} represent the peak load demand and converter efficiency, respectively. The converter with a life span of 20 years and a round-trip efficiency of 90% is considered in this study. The converter capital cost and replacement cost are 116 $/kW each, whereas the Operation and Maintenance (O&M) cost is considered as 3 $/kW/year during the simulation [40].

Battery: The battery is an essential component of a microgrid system as it provides energy storage and enables the system to operate independently of the utility grid. The energy delivered from a battery can be expressed by the following equations as follows [41]:

$$E_{\text{bat}} = E_{\text{bat}}^{0} + \int_{0}^{t} V_{\text{bat}} I_{\text{bat}} \, \mathrm{d}t, \tag{9}$$

where E_{bat}^{0} denotes the initial battery charge, V_{bat} are I_{bat} the voltage and current of the battery, respectively [37]. To determine the correct value of battery energy, it is necessary to precisely estimate the SOC. The SOC of the battery fluctuates over time, and this can be mathematically represented by equation 10:

$$\frac{\text{SOC}(t)}{\text{SOC}(t-1)} = \int_{T-1}^{T} \frac{P_{\text{bat}}(t)\eta_{\text{bat}}}{V_{\text{bus}}} \, \mathrm{d}t. \tag{10}$$

The following equation can be used to calculate the maximum power rating of the battery.

$$P_{\text{bat}}^{\text{max}} = \frac{N_{\text{bat}} V_{\text{bat}} I_{\text{bat}}^{\text{max}}}{1000}, \tag{11}$$

where, N_{bat}, represents the number of batteries, V_{bat}, represents the voltage rating of a single battery, and I_{bat} represents the maximum charging current rating in Amperes[41, 43]. The flat plate Li-ion battery's maximum state of charge is taken as 100% while the minimum state of charge is taken as 10%, respectively in this study. A 90% round-trip efficiency of the battery is considered in this study [41]. The 243 $/kW is taken as the capital cost and 200 $/kW as the replacement cost of the battery, while the O&M cost in the present study is taken as 0.50 $/year [44].

Grid: Grid connection of microgrids is helpful to increase the use of renewable energy sources, reduce emissions, and promote economic development. When the microgrid generates more electricity than it needs, it can export the excess back to the utility grid, and the utility will pay the microgrid for this electricity. This can provide a source of revenue for the microgrid, and it can also help to stabilize the utility grid by providing additional capacity during times of high demand. The microgrid is connected to the local grid to sell the excess electricity generated by RES. The electricity sell-back price to the grid considered as 0.080 $/kWh during the analyses.

Evaluation Criteria of microgrid system: The Total Net Present Cost (TNPC) is a measure of the present value of all costs associated with the system over its lifetime, minus any revenues that are generated by the system. HOMER calculates the total cost of the system, including capital costs, operations and maintenance costs, and fuel costs. The TNPC of the microgrid system is calculated as per the following equation 12.

$$TNPC = \frac{C_A}{CRF}. \tag{12}$$

C_A and CRF represent the total annualized cost ($/year) and the capital recovery factor, respectively [41]. CRF can further be estimated as:

$$CRF = \frac{i(1+i)^n}{(1+i)^n - 1}. \tag{13}$$

The nominal interest rate (%) which depends on the yearly inflation rate is represented by 'i', whereas the project lifetime in years is represented by n [41, 45].

The per-unit Cost Of Energy (COE) represents the cost of producing and delivering one unit of energy, such as one kilowatt-hour (kWh) of electricity, over the lifetime of the system. It is calculated by dividing the total annualized cost ($/year) of the system by the total amount of energy produced over its lifetime and represented by the following equation:

$$COE = \frac{C_A}{E_T}, \tag{14}$$

where E_T represents the total electrical demand served in kWh/ year [41].

2.2. Micro-grid Operation Stage Model

After determining the appropriate sizing of microgrid components such as BESS, converter, WT, and PV modules based on the location and loads in stage one, the second stage evaluates the performance of the designed system under extreme weather conditions as a worst-case scenario. As shown in Figure 1b, the system is controlled by an MPC, which is responsible for determining the optimal usage of the battery to ensure resilient operation while considering battery longevity.

The Laila cyclone, which occurred between May 16 and 26, 2010 at the village near the coastal city of Ongole in Andhra Pradesh, India is selected for this. Weather data from this period is used to determine generation, and load data is also presented for the same timeframe. Figure 4 shows the consumption patterns of different load types, including essential, business, and deferred loads, along with the total load demand over time during a specific time of the HILP event. Figure 5 illustrates the wind speed measured at 10 meters and 50 meters, along with the generated wind power. Since the WT hub is at a height of 50 meters, the wind speed at the hub height is scaled up using the Equation 6.

In this equation, α is the Hellmann exponent, which is equal to 0.27 for unstable air above human-inhabited areas. The wind speed values measured are hourly averages, meaning that when the speed reaches 20 m/s, there could be moments within the hour when wind speeds exceed 25 m/s. To better protect the infrastructure during the peak of

a cyclone, the cut-off threshold for wind turbine operation is set to 20 m/s, ensuring turbines are shut down before extreme wind speeds occur. This adjustment is applied only for the hours immediately before and after the peak wind speeds of the cyclone, rather than for the entire time horizon. The wind generation is then calculated using the windpowerlib library in Python [46].

For solar generation, the Plane of Array (POA) global irradiance is calculated, and the total solar generation is determined using the pvlib library [47], as shown in Figure 6. Figure 7 illustrates the power generation from PV panels and WT during the Cyclone. The total renewable generation, represented by the magenta line, highlights the fluctuations in power output due to variations in solar irradiance and wind speed throughout the event. Additionally, the total load demand and generation during the HILP event are illustrated in Figure 8.

One advantage of using wind and solar generation in suitable locations is their ability to complement each other in terms of generation. Wind generation typically occurs during the night, while solar generation peaks during the day. Additionally, before and after events like cyclones or storms, wind generation tends to be higher due to the characteristics of these phenomena. Even when high wind speeds cause the wind turbine to shut down due to cut-off speeds, there is still some minor PV generation, primarily due to the cloudy weather conditions.

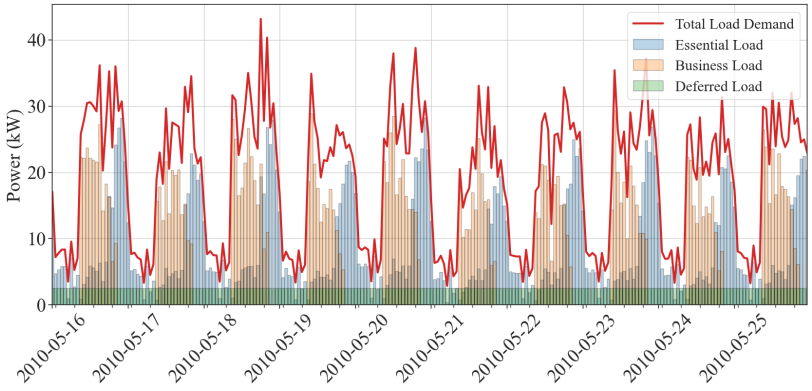

Figure 4: Load consumption patterns for different load types during Cyclone Laila.

2.2.1. General Overview of the Model

An MPC control strategy of the microgrid based on a resiliency index is proposed, which will be detailed in the following section. This control scheme is illustrated in Figure 9. As shown, when the system's resiliency falls below a threshold such as 95%, the limitations on SOC and battery life considerations can be relaxed. In these extreme situations, prioritizing the fulfillment of essential loads takes precedence. Additionally, before the end of the 10-day period, the operational point for each hour is determined based on the next 24 hours in the MPC model.

As shown in Figure 10, the first step involves determining the control variables for the next 24 hours. This includes

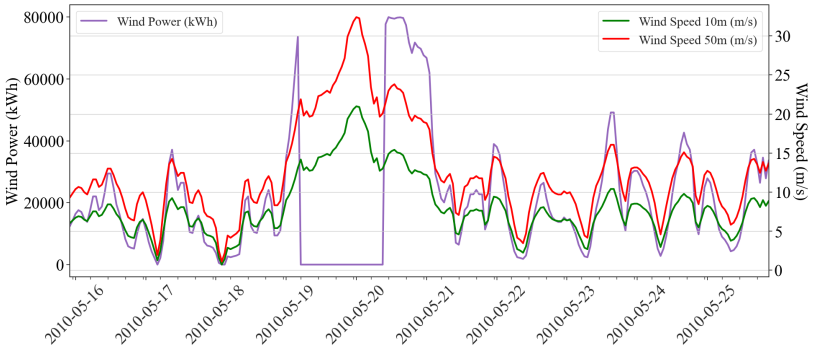

Figure 5: Wind speed at different heights (10m and 50m) and the corresponding wind power generation during Cyclone Laila.

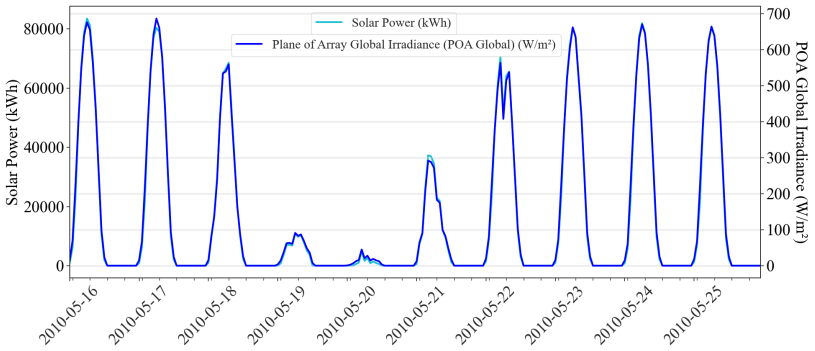

Figure 6: Solar power generation and POA global irradiance during Cyclone Laila.

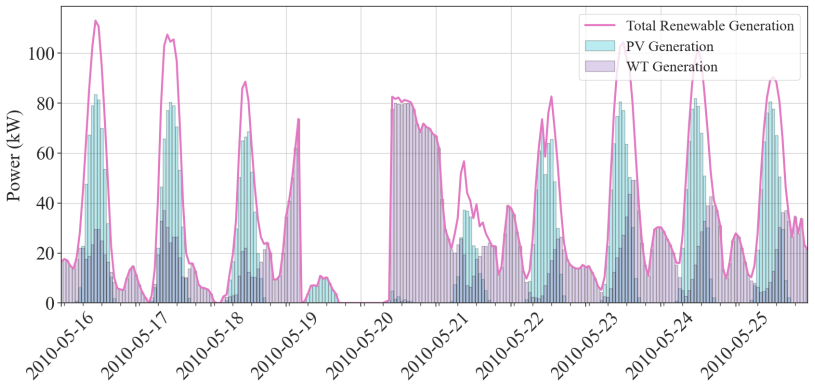

Figure 7: PV and WT generations during Cyclone Laila.

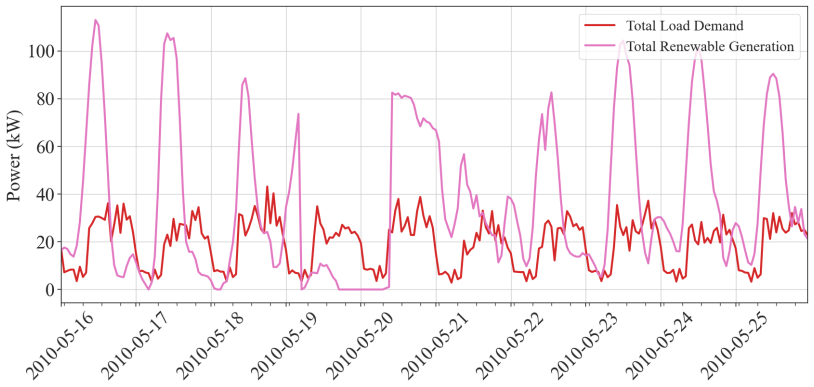

Figure 8: Total load and generations during Cyclone Laila.

deciding the BESS modes (charging, discharging, or idle), managing the SOC, and implementing demand response for loads. After this, the process moves to the next hour, represented by the green box, where the optimal solution for that time step is calculated by solving the MILP problem. This sliding window approach continues until the end of day 9. To make decisions for the last hour of day 9, data for day 10 is required to cover the next 24 hours.

2.2.2. Mathematical Representation

In this section, the mathematical optimization behind the MILP problem in the MPC model will be discussed.

Let A, K, and B be three sets defined as written in Equation 15. The set A represents the battery modes, which can be charging, discharging, or idle. The set K represents the 24-hour window time of the MPC model. The set B represents the line numbers of the piecewise parts of the Battery Life Cycle (BLC) - Depth of Discharge (DOD) curve, as the non-linear curve is divided into 8 parts.

$$\text{Set } A : \{\text{'CH'}, \text{'DIS'}, \text{'IDLE'}\} \tag{15a}$$

$$\text{Set } K : \{1, 2, 3, \ldots, 24\} \tag{15b}$$

$$\text{Set } B : \{1, 2, 3, \ldots, 8\}. \tag{15c}$$

Parameters and variables of MILP optimization are listed in Tables 2 and 3. It is important to note that "$^-$" symbol is used for auxiliary variables in the process of linearization.

Equation 16 shows how the battery SOC is updated each hour, leading to the SOC for the next hour.

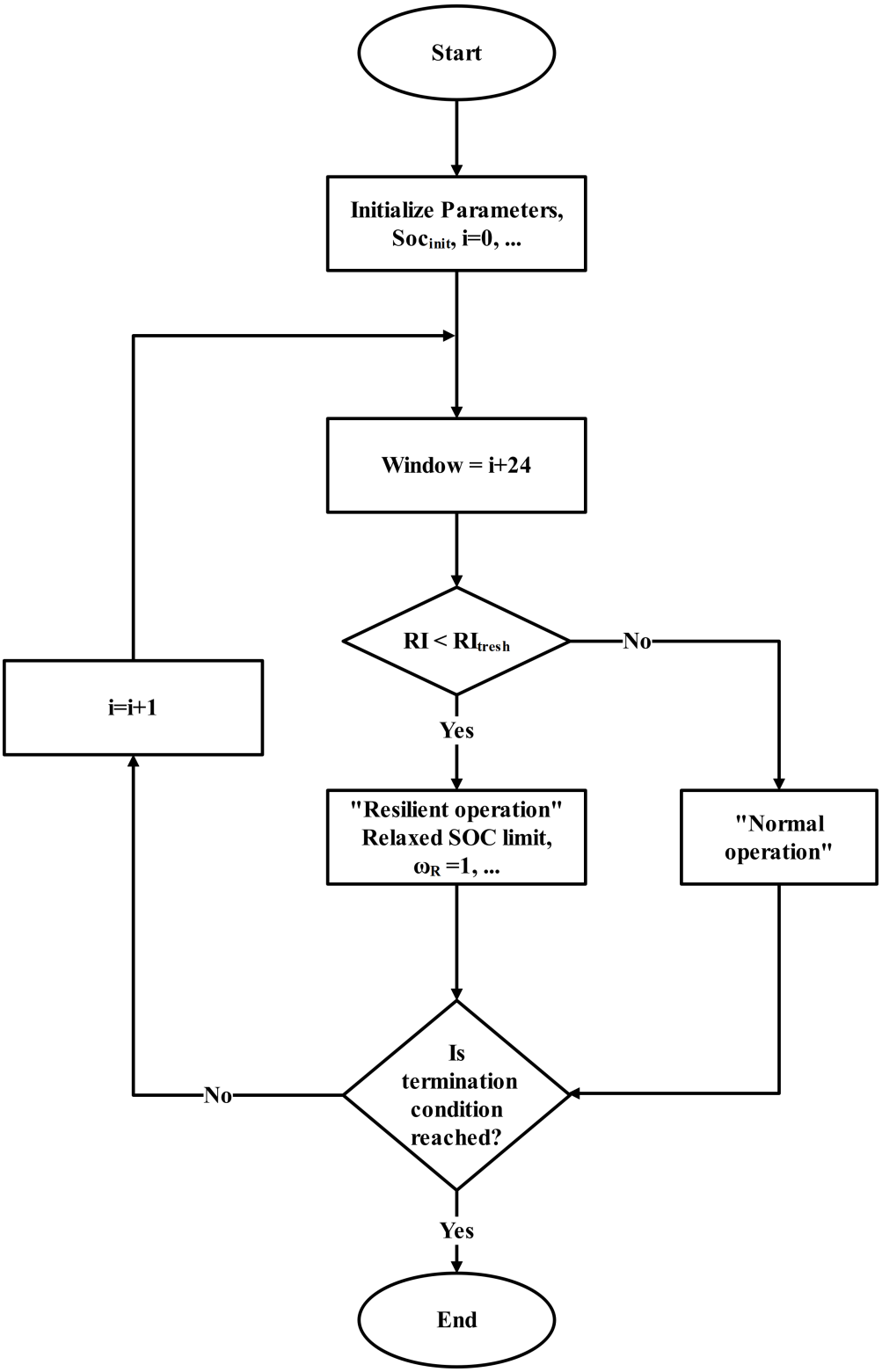

Figure 9: Flowchart of the smart resilient control strategy for microgrid operation.

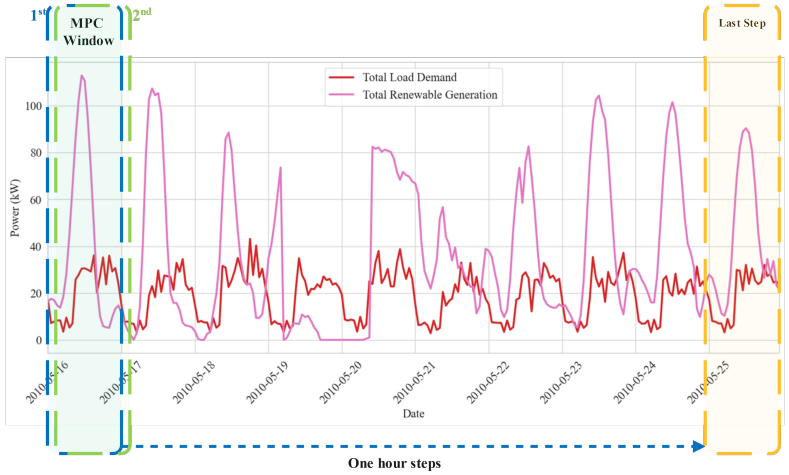

Figure 10: Proposed MPC sliding window.

Table 2: List of parameters and their definition.

Parameters	Definition	Parameters	Definition
Load_1	Essential Loads (kW)	RE_{Gen}	Total Renewable Generation (kW)
Load_2	Business Loads (kW)	η_{ch}	Charging Efficiency
Load_3	Agricultural Loads (Deferred Loads) (kW)	η_{dis}	Discharging Efficiency
ω_{bat}	Weighting Factor for Minimizing Total Switching	ω_t	Weighting Factor for Minimizing Total Imbalance
ω_R	Weighting Factor for Minimizing Total Unserved Loads	ω_{BLC}	Weighting Factor for Maximizing Battery Life Cycle
$w_{Essential}$	Prioritizing Factor of Essential Loads	$w_{Business}$	Prioritizing Factor of Business Loads
$w_{Deferred}$	Prioritizing Factor of Deferred Loads	BigM	Big M Factor for Linearization
SOC_{init}	Initial State of Charge	C_{bat}	Cost of Battery ($/kWh)
Cycles_{bat}	Number of Battery Cycles with 100% DOD	C_{CH-DIS}	Cost of each Charging and Discharging ($)
C_{idle}	Cost of IDLE Mode ($)	P_{bat}^{min}	Minimum Capacity of Battery Converter (kW)
P_{bat}^{max}	Maximum Capacity of Battery Converter (kW)	P_{bat}^{cap}	Maximum Capacity of Battery (kWh)
DR_1	Allowed Shifting Essential Load (kW)	DR_2	Allowed Shifting Business Load (kW)
DR_3	Allowed Shifting Deferred Load (kW)	$\text{P}_{DR-Diff_1}$	Demand Response Differences from Each Iteration for Essential Load (kW)
$\text{P}_{DR-Diff_2}$	Demand Response Differences from Each Iteration for Business Load (kW)	$\text{P}_{DR-Diff_3}$	Demand Response Differences from Each Iteration for Deferred Load (kW)
Coefficients	Linearized BLC Curve Coefficients	ranges	Different Ranges of Linearized BLC Curve

$$SOC(k+1) \times P_{bat}^{cap} = SOC(k) \times P_{bat}^{cap} + \eta_{ch} \times \bar{P}_{bat}(\text{'CH'}, k) - \frac{\bar{P}_{bat}(\text{'DIS'}, k)}{\eta_{dis}}. \tag{16}$$

Since the battery must operate in one of its modes each hour, this requirement is managed by the δ function as described in Equation 17a. Also, the Big-M method is used in Equations 17c to linearize Equation 17b. Here, the Big-M value is set to correspond to the maximum physical limit of the converter (52 kW), and wherever Big-M values are used throughout the article, they are selected to be sufficiently large to reflect the maximum physical constraints of the relevant components [48].

Table 3: Variables and their definitions

Variables	Definition	Variables	Definition
P_s(k)	Total Power Supply at Hour k (kW)	SOC(k)	State of Charge $(0.2, 0.9)$ for Deferred Loads at Hour k
P_{s_1}(k)	Power Supply for Essential Loads at Hour k (kW)	SOC(1)	SOC_{init}
P_{s_2}(k)	Power Supply for Business Loads at Hour k (kW)	$\delta(A, k)$	Showing different Battery Operation Modes at Hour k
P_{s_3}(k)	Power Supply for Deferred Loads at Hour k (kW)	$P_{bat}(A, k)$	Battery Power $(P_{bat_{min}}, P_{bat_{max}})$ at Hour k (kW)
$\bar{P}_{bat}(A, k)$	Auxiliary Variable for Linearizing $P_{bat}(A, k)$ (kW)	BLC(B, k)	BLC at Hour k
$\sigma(A, A, k)$	Transition of Battery Modes at Hour k	$\delta_{BLC}(B, k)$	Different Linear Equation Lines of BLC Curve at Hour k
P_{Imb_1}(k)	Power Imbalance for Essential Loads at Hour k (kW)	δ_{Imb_1}(k)	Binary for Negative Imbalances in Essential Loads at Hour k
P_{Imb_2}(k)	Power Imbalance for Business Loads at Hour k (kW)	δ_{Imb_2}(k)	Binary for Negative Imbalances in Business Loads at Hour k
P_{Imb_3}(k)	Power Imbalance for Deferred Loads at Hour k (kW)	δ_{Imb_3}(k)	Binary for Negative Imbalances in Deferred Loads at Hour k
$\bar{P}_{Imb_1}$(k)	Negative Imbalance for Essential Loads at Hour k (kW)	DR_1(k)	Demand Response Ratio for Essential Loads at Hour k
$\bar{P}_{Imb_2}$(k)	Negative Imbalance for Business Loads at Hour k (kW)	DR_2(k)	Demand Response Ratio for Business Loads at Hour k
$\bar{P}_{Imb_3}$(k)	Negative Imbalance for Deferred Loads at Hour k (kW)	DR_3(k)	Demand Response Ratio for Deferred Loads at Hour k
P_{DR_1}(k)	Essential Loads after Demand Response at Hour k (kW)	DR_{Change_1}(k)	Changes in Essential Loads after Demand Response at Hour k (kW)
P_{DR_2}(k)	Business Loads after Demand Response at Hour k (kW)	DR_{Change_2}(k)	Changes in Business Loads after Demand Response at Hour k (kW)
P_{DR_3}(k)	Deferred Loads after Demand Response at Hour k (kW)	DR_{Change_3}(k)	Changes in Deferred Loads after Demand Response at Hour k (kW)
J_{bat}(k)	Cost of Battery Switching at Hour k	J_t(k)	Cost of Power Imbalances at Hour k
J_R(k)	Cost of Resiliency Index at Hour k	J_{BLC}(k)	Cost of BLC at Hour k

$$\delta(\text{'CH'}, k) + \delta(\text{'DIS'}, k) + \delta(\text{'IDLE'}, k) = 1 \tag{17a}$$

$$\bar{P}_{bat}(a, k) = \delta(a, k) \times P_{bat}(a, k) \tag{17b}$$

$$\begin{cases} \delta(\text{'CH'}, k) + \delta(\text{'DIS'}, k) + \delta(\text{'IDLE'}, k) = 1 \\ \bar{P}_{bat}(a, k) \leq BigM \times \delta(a, k) \\ \bar{P}_{bat}(a, k) \geq -BigM \times \delta(a, k) \\ \bar{P}_{bat}(a, k) - P_{bat}(a, k) \leq BigM \times (1 - \delta(a, k)) \\ \bar{P}_{bat}(a, k) - P_{bat}(a, k) \geq -BigM \times (1 - \delta(a, k)). \end{cases} \tag{17c}$$

To determine the transition between battery states, referred to as switching in this paper, Equation 18 is used. This equation is applicable when $\alpha \neq \beta$ and $k > 1$. In this context, σ represents the state transitions.

$$\begin{cases} \sigma(\alpha,\beta,k) \geq \delta(\alpha,k-1) + \delta(\alpha,\beta-1) - 1 \\ \sigma(\alpha,\beta,k) \leq \delta(\alpha,k-1) \\ \sigma(\alpha,\beta,k) \leq \delta(\beta,k-1). \end{cases} \tag{18}$$

Now, the first part of the objective function, related to the cost of switching, can be introduced as in Equation 19.

$$\begin{aligned} J_{\text{bat}}(k) = \sum_{k\in K} \frac{C_{\text{bat}}}{Cycles_{\text{bat}}} & \left(\delta(\text{'CH'},k) + \delta(\text{'DIS'},k)\right) \\ & + C_{\text{CH-DIS}}\left(\sigma(\text{'CH'},\text{'DIS'},k) + \sigma(\text{'DIS'},\text{'CH'},k)\right) \\ & + C_{\text{idle}}\big(\sigma(\text{'IDLE'},\text{'DIS'},k) + \sigma(\text{'DIS'},\text{'IDLE'},k) \\ & \qquad + \sigma(\text{'IDLE'},\text{'CH'},k) + \sigma(\text{'CH'},\text{'IDLE'},k)\big). \end{aligned} \tag{19}$$

Figure 11a shows that the BLC curve is non-linear with a lower DOD that suggests a longer battery life. However, in order to remain consistent with linear programming, the curve is linearized as shown in Figure 11b. Equation 20 provides the piecewise linear approximations.

$$y = \begin{cases} -25.35\,x + 5535, & 80 \leq x \leq 100 \\ -39.1\,x + 6635, & 60 \leq x < 80 \\ -70.4\,x + 8513, & 40 \leq x < 60 \\ -177.9\,x + 12813, & 20 \leq x < 40 \\ -578\,x + 20815, & 10 \leq x < 20 \\ -1878\,x + 33815, & 5 \leq x < 10 \\ -12732.75\,x + 88088.75, & 1 \leq x < 5 \\ -324644\,x + 400000, & 0 \leq x < 1. \end{cases} \tag{20}$$

To select the appropriate line, it is necessary to write the Equations from 21 to 26. Equation 22 introduces a set of binary variables, divided into 8 parts, where their summation should equal the battery's discharge state. This means that if one of the binary variables representing discharge is 1, then one of the corresponding δ_{BLC} should also be 1. To maintain linearity in the problem, Equations 23 and 24 are introduced using the Big-M method. Additionally, Equation 21 is used to determine the BLC for all 8 segments. To find the BLC for a specific segment, $B\bar{L}C(b,k)$ is introduced. With these equations, the second part of the objective function can be introduced, relating to the battery

life cycle in Equation 26. It is worth mentioning that $B\bar{L}C(b,k)$ is normalized based on the upper coefficient of its piecewise linear segment.

To illustrate this set of equations, consider an example where at hour 5, there is a discharge with a DOD of 30%. According to equation 22, $\delta(\text{'DIS'},5)$ equals one, meaning the summation of all $\delta_{BLC}(b,5)$ should be equal to one. Consequently, one of the eight δ_{BLC} variables should be one. From equations 23 and 24, it is ensured that $\delta_{BLC}(4,5)$ takes the value of one, while the other δ_{BLC} values are zero at hour 5. This means that $BLC(b,5)$ will use the line formula related to its segment. However, equation 21 calculates other sections where δ_{BLC} is zero as well. To address this issue, $B\bar{L}C$ is introduced in Equation 25 to ensure that only the dedicated section is considered in the objective function. Therefore, $B\bar{L}C(4,5)$ will take the appropriate value in this case.

$$\begin{aligned} BLC(b,k) = {} & \frac{\bar{P}_{\text{bat}}(\text{'DIS'},k)}{P^{\text{cap}}_{\text{bat}}} \times \text{coefficients}(b,1) \\ & + \delta_{\text{BLC}}(b,k) \times \text{coefficients}(b,2) \\ & + (1-\delta_{\text{BLC}}(b,k)) \times \text{coefficients}(8,2). \end{aligned} \tag{21}$$

$$\sum_{b\in B} \delta_{BLC}(b,k) = \delta(\text{'DIS'},k). \tag{22}$$

$$\begin{aligned} \frac{\bar{P}_{\text{bat}}(\text{'DIS'},k)}{P^{\text{cap}}_{\text{bat}}} \times 100 \geq {} & \text{ranges}(b,1) \times \delta_{\text{BLC}}(b,k) \\ & - \text{BigM} \times (1-\delta_{\text{BLC}}(b,k)). \end{aligned} \tag{23}$$

$$\begin{aligned} \frac{\bar{P}_{\text{bat}}(\text{'DIS'},k)}{P^{\text{cap}}_{\text{bat}}} \times 100 \leq {} & \text{ranges}(b,2) \times \delta_{\text{BLC}}(b,k) \\ & + \text{BigM} \times (1-\delta_{\text{BLC}}(b,k)). \end{aligned} \tag{24}$$

$$\begin{cases} -\delta_{BLC}(b,k) \times \text{BigM} \leq B\bar{L}C(b,k) \\ B\bar{L}C(b,k) \leq \delta_{BLC}(b,k) \times \text{BigM} \\ B\bar{L}C(b,k) - BLC(b,k) \leq (1-\delta_{BLC}(b,k)) \times \text{BigM} \\ -(1-\delta_{BLC}(b,k)) \times \text{BigM} \leq B\bar{L}C(b,k) - BLC(b,k). \end{cases} \tag{25}$$

$$J_{BLC}(k) = \sum_{b \in B} B\bar{L}C(b,k). \tag{26}$$

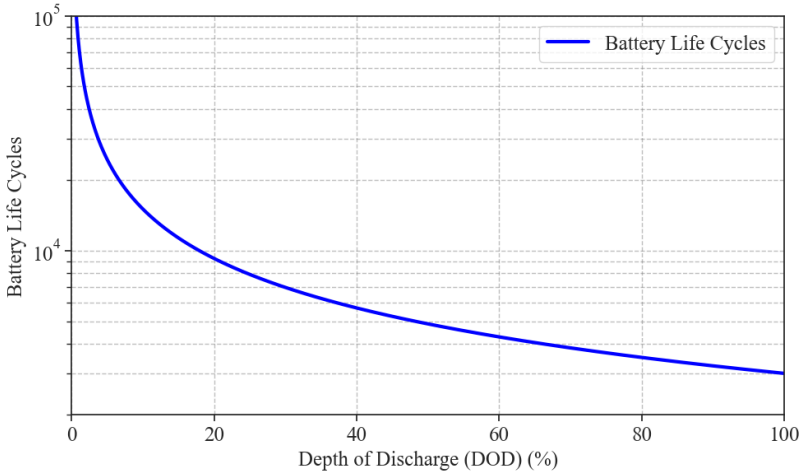

(a)

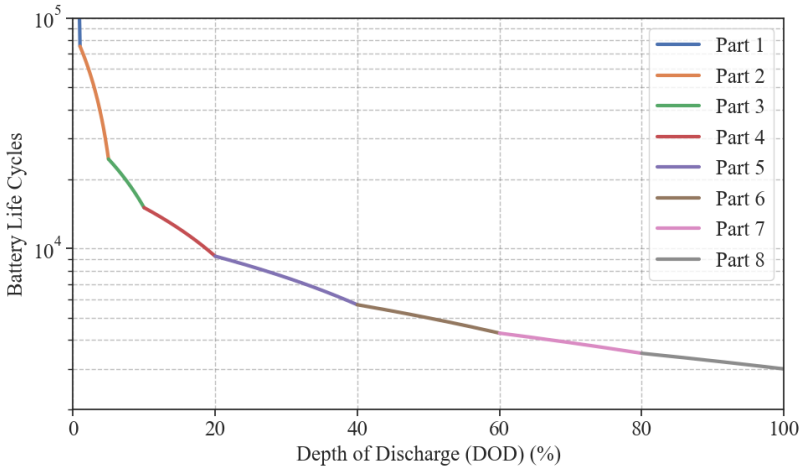

(b)

Figure 11: Comparison of BLC-DOD curves: (a) Non-linear curve, (b) linear curve.

Before discussing how the loads are supplied, it is important to introduce the concept of demand response formulated in Equation 27. Shiftable loads are considered for demand response, meaning the total load in each 24-hour period should remain consistent before and after the demand response is applied. Given that MPC updated in one-hour steps, $P_{DR-Diff}$ is included in the equation to reduce the effect of mismatches. Additionally, as the model horizon is extended, this mismatch becomes negligible.

$$\begin{cases} P_{DR}(k) = \mathrm{DR}_{Change}(k) + \mathrm{Load}(k) \\ \mathrm{DR}_{Change}(k) = \mathrm{DR}(k) \times \mathrm{Load}(k) \\ \sum_{k \in K} \mathrm{DR}_{Change}(k) + P_{DR-Diff} = 0. \end{cases} \tag{27}$$

Now, Equation 28 can be introduced to illustrate the power supply for demands. The supply consists of the sum of renewable generations and battery discharges, while battery charging is considered as a negative part. Three different lines are assumed for each load category to determine power imbalances, both positive and negative. Positive imbalances indicate an excess of energy that cannot be stored in the battery due to either limitations or decisions made by the MILP problem.

$$\begin{cases} P_s(k) = RE_{Gen}(k) + \bar{P}_{bat}(\text{'DIS'}, k) - \bar{P}_{bat}(\text{'CH'}, k) \\ P_s(k) = P_{s_1}(k) + P_{s_2}(k) + P_{s_3}(k) \\ P_{s_{Load}}(k) = P_{DR_{Load}}(k) + P_{Imb_{Load}}(k) \\ P_{Imb}^{Total}(k) = \sum_{Load=\{1,2,3\}} \bar{P}_{Imb_{Load}}(k). \end{cases} \tag{28}$$

With the previously mentioned equations, the third part of the objective function, related to power imbalances, can now be introduced as in Equation 29. Although this equation includes a quadratic term, it is still considered as MILP, or more accurately, as Mixed-Integer Quadratic Programming (MIQP), which the Gurobi solver can handle.

$$J_t(k) = \sum_{k \in K} \left(P_s(k) - P_{DR_{Load}}(k) \right)^2. \tag{29}$$

To determine the final part of the objective function, the negative imbalances must first be identified. This is achieved by introducing the set of equations in Equation 30.

$$
\begin{cases}
-P_{Imb_{Load}}(k) \leq \bar{P}_{Imb_{Load}}(k) \\
-\delta_{Imb_{Load}}(k) \times \text{BigM} \leq \bar{P}_{Imb_{Load}}(k) + P_{Imb_{Load}}(k) \\
\bar{P}_{Imb_{Load}}(k) + P_{Imb_{Load}} \leq \delta_{Imb_{Load}}(k) \times \text{BigM} \\
-(1 - \delta_{Imb_{Load}}(k)) \times \text{BigM} \leq \bar{P}_{Imb_{Load}}(k) \\
\bar{P}_{Imb_{Load}}(k) \leq (1 - \delta_{Imb_{Load}}(k)) \times \text{BigM} \\
P_{Imb_{Load}}(k) \leq \text{BigM} \times \delta_{Imb_{Load}}(k) \\
-P_{Imb_{Load}}(k) \leq \text{BigM} \times (1 - \delta_{Imb_{Load}}(k)).
\end{cases} \tag{30}
$$

By prioritizing the loads based on their assigned weightings, the resiliency index can now be introduced as the final part of the objective function.

$$
J_R(k) = \sum_{k \in K} 1 - \frac{\sum_{Load=1,2,3}(w_{Load} \times \bar{P}_{Imb_{Load}}(k))}{\sum_{Load=1,2,3}(w_{Load} \times P_{Load})}. \tag{31}
$$

With all the components in place, the Objective Function (OF) can now be introduced as shown in Equation 32. The coefficients applied to each term are used to normalize them between 0 and 1.

$$
\begin{aligned}
OF = \sum_{k \in K} \frac{\omega_{bat} \times J_{bat}(k) \times 14.45}{24} - \frac{\omega_{BLC} \times J_{BLC}(k)}{24} \\
+ \frac{\omega_t \times J_t(k)}{24 \times 1600} - \frac{\omega_R \times J_R(k)}{24}.
\end{aligned} \tag{32}
$$

After the optimization process ends, several metrics are calculated for comparison purposes. To determine the overall Resilience Index (RI) across the entire study horizon, Equation 33 is applied. This equation is analogous to Equation 31, with the key difference being that RI is computed over the entire time horizon rather than within a 24-hour sliding window.

$$
RI = \sum_{TimeFrame} 1 - \frac{\sum_{Load=1,2,3}(w_{Load} \times \bar{P}_{Imb_{Load}})}{\sum_{Load=1,2,3}(w_{Load} \times P_{Load})}. \tag{33}
$$

The calculation of the Expected Years (EY) is conducted using Equation 34. The process involves first determining the BLC for each instance of battery discharge, considering that BLC is a function of the DOD. The EY is then derived

by factoring in the number of days over which the optimization is performed.

$$EY = \left(\frac{1}{\sum_{i=1}^{n_{\text{dis}}} \frac{1}{\text{BLC(DOD\%)}}} \right) \times \left(\frac{n_{\text{Days}}}{365} \right). \tag{34}$$

The Total number of Switches (TS) across the study horizon is calculated using Equation 35. This involves summing the switching events over the entire period.

$$TS = \sum_{i \in \{\text{CH,DIS,IDLE}\}} \sum_{\substack{j \in \{\text{CH,DIS,IDLE}\} \\ i \neq j}} \sigma(i, j). \tag{35}$$

3. Simulation Results and Discussions

This section provides a detailed overview of both the planning and operational analyses executed for the proposed microgrid system. The planning analysis focuses on the optimal design and sizing of the microgrid components and the operational analysis evaluates the resilience of the system operation under HILP events.

3.1. Planning Results and Discussion

The optimal sizing of the various components of the MG system has been evaluated considering the actual solar and wind resources data and realistic load demand of the village situated at a location in Andhra Pradesh, India. The microgrid system comprises PV, and WT as generating sources, a converter for conversion of AC/DC energy demand, and batteries are connected to balance the energy demand of the load. Two case studies have been considered in which the microgrid operates in an isolated mode in case-1 and the grid-connected mode to sells excess electricity in case-2. The analysis encompasses simulation results showcasing the generation response of various components, and cost evaluations of the overall system setup. The investigation was carried out using HOMER Pro version 3.14 software, employing a Load-Following (LF) dispatch strategy for the studied microgrid systems. The lifetime of the project is 20 years and the expected inflation rate is considered as 2.0% during the simulation.

Table 4 shows the optimal sizing of the generators and other components, operating cost per year, total net present cost, cost of electricity, renewable fractions, electricity production by PV and WG, and excess electricity of the system in the isolated and grid-connected mode of the MG system. The optimal configuration for the MG system, which combines PV and WT generation units with battery storage, includes an 80-kW generic wind generator, a 140-kW generic flat-plate PV system, a 52-kW system converter, and 780 generic lithium-ion batteries, each with a rated capacity of 1 kWh for both isolated(case-1) and grid-connected (case-2) systems. This configuration operates under a load-following (LF) dispatch strategy. The analysis gives a TNPC of $494093, a COE of $0.237 per kWh, and an

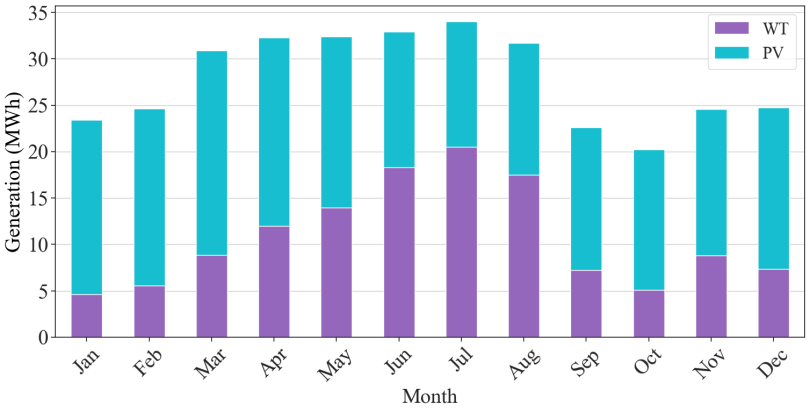

Figure 12: Power generation response of solar and wind units.

operating cost of $8849 per year for the isolated MG system (case-1), with RESs contributing 100% to the energy generation. The cost parameters of the MG system operating in grid-connected mode (case-2) comprise a TNPC of $442701, a COE of $0.163 per kWh, and an operating cost of $4411 per year with RESs contributing 100% to the energy generation. The grid-connected microgrid system doesn't buy energy from the grid and only sells surplus electricity to the grid, generating revenue that offsets the overall cost of electricity. As a result, the COE for the grid-connected microgrid system is $0.163 per kWh, compared to $0.237 per kWh for an isolated microgrid system.

Table 4: Techno-economic performance parameters of the microgrid system.

Components/ Case	PV/ (kW)	WG/ (kW)	Batteries/ (Units)	Converter/ (Units)	Total/ NPC ($)	Operation Cost ($/year)	COE/ ($/kWh)
	140kW	80kW	780kWh	52kW	$494093	$8849	$0.237
	140kW	80kW	780kWh	52kW	$442701	$4411	$0.163

Components/ Case	Initial Cost ($)	Renewable Fraction(%)	Grid Connection	WG Generation (kWh/year)	PV Generation (kWh/year)	Excess Electricity
	$391624	100%	No	129825	204600	43.5%
	$391624	100%	Yes	129825	204600	25%

The generating units effectively meet the village's load demand throughout the year in which excess energy from RESs is used to charge the battery unit, ensuring a continuous power supply when needed. Figure 12 shows the power generation response of both solar and wind-based generating units over the year. The total power production is 334,425 kWh annually, with the PV units generating 204,600 kWh (61.2%) and the wind units producing 129,825 kWh (38.8%). The wind generator demonstrates peak performance during June and July due to optimal wind speeds, as depicted in Figure 12. During other times, the PV generator compensates for the power demand. The battery unit plays a crucial role in managing the variability of renewable energy resources by storing generated energy and supplying it when needed. The battery has a nominal capacity of 780 kWh and an annual throughput of 64,949 kWh, with daily throughput details shown in Figure 13. This ensures that the battery bank can satisfy load demand even

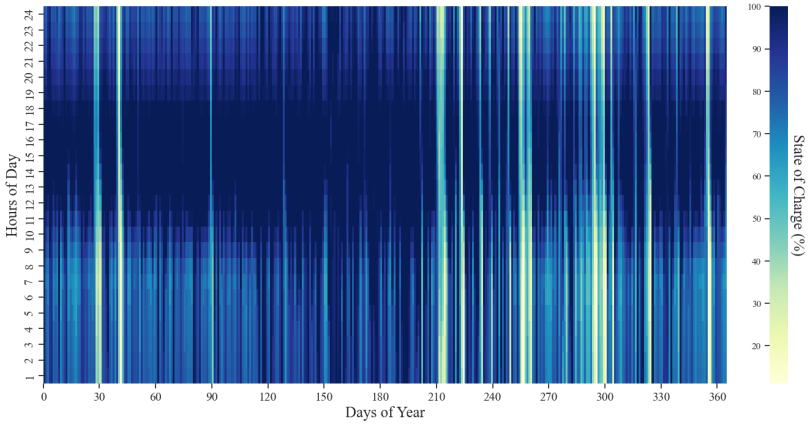

Figure 13: Battery utilisation through the year.

when RES generation is unavailable, providing a continuous power supply to end users. While this study primarily focuses on cyclone-prone coastal India, the methodology can be tailored to different climatic conditions, regulatory structures, and economic contexts by adjusting input data, battery parameters, and local energy tariffs.

The sensitivity analyses have also been conducted to provide valuable insights and to evaluate the economic resilience of the microgrid design. The fluctuations in key economic parameters can influence the overall system performance and cost-effectiveness. The reduction in capital cost of the generators due to subsidies, competition, market conditions, or policy adjustments and increment in initial capital cost of the generators due to supply chain constraints or technological advancements that lead to higher production costs can severely impact the economic feasibility of overall microgrid system. The sensitivity analyses considering the variations in the capital cost of PV, WTG, battery and grid sell back prices with respect to key economic parameters, such as the COE ($/kWh) initial investment cost, and the total NPC of the proposed microgrid system are shown in Figure 14a and Figure 14b. The microgrid requires a 140-kW solar PV system with a capital cost of $741/kW. The sensitivity analysis reveals that if the capital cost of the PV system fluctuates between half (0.5) and double (2) from its initial value, as a result of factors such as system subsidies, market competition, technological advancements, scarcity of solar PV systems, or rising costs due to new manufacturing technologies, this can significantly affect the system's economics. Specifically, the initial cost of the PV system would range from $339,754 to $495,364, while the total NPC would vary from $390,830.50 to $546,440.50 as shown in Figure 14a. Correspondingly, the COE ($/kWh) would change from $0.1435 to $0.2006, respectively.

Additionally, the proposed microgrid requires an 80-kW WTG with a capital cost of $11,539 per 10 kW. The sensitivity analysis shows that variations in the capital cost of the WTG led to changes in the system's financial parameters. Specifically, the initial cost of the WTG would range from $345,468 to $483,936, the total NPC would fluctuate between $396,544.50 and $535,012.50, and the COE would range from $0.1456 to $0.1964 per kWh as

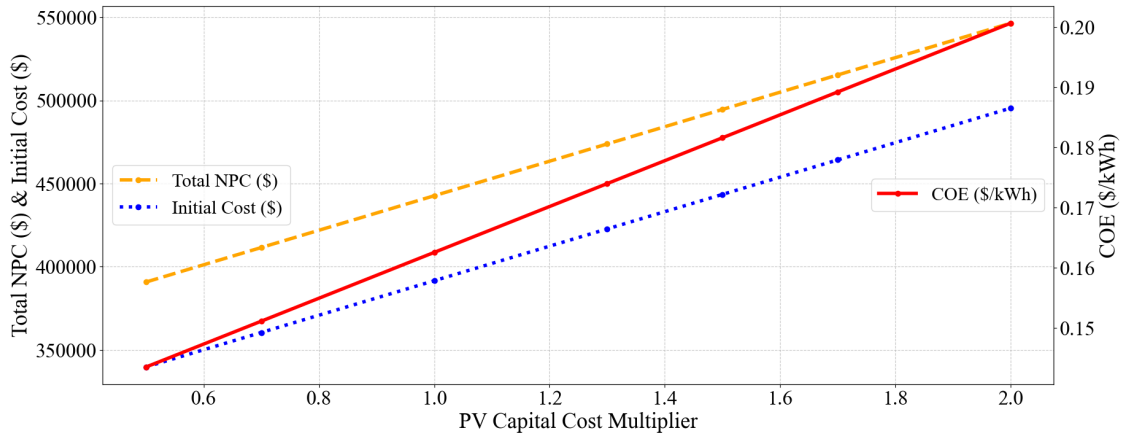

(a)

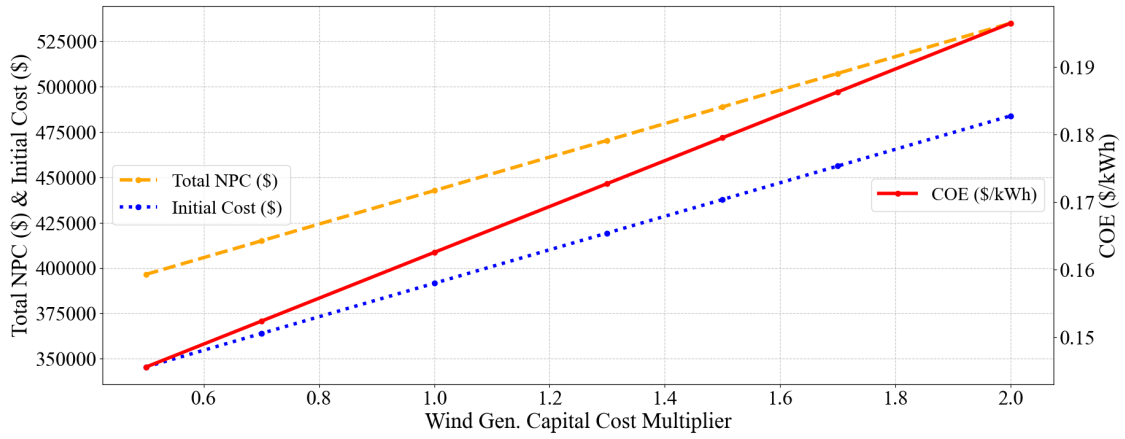

(b)

Figure 14: Key economic indicators due to fluctuations in renewable generator's cost (a) PV generator capital cost, (b) wind generator capital cost.

depicted in Figure 14b. These changes are driven by variations in the initial capital cost of the WTG.

The impact of fluctuations in key economic indicators, such as COE in $/kWh, total NPC, and changes in battery and grid sellback prices, is illustrated in Figure 15a and Figure 15b. Variations in the initial capital cost of the battery directly influence the initial system cost, total NPC, and the COE for the microgrid system. Specifically, Figure 15a shows how changes in battery capital prices affect these parameters. Sensitivity analysis demonstrates that all costs are sensitive to fluctuations in battery capital costs. The microgrid system requires 780 kWh of battery storage, with a capital cost of $243 per kW for each battery. As the battery cost varies, the system's initial cost fluctuates between $296,854 and $581,164, the total NPC varies from $347,930.50 to $632,240.50, and the COE ranges from $0.1277 to $0.2321 per kWh. These changes occur when the battery cost shifts from half to double the original capital cost due to future market conditions. Figure 15b shows the influence of electricity sell-back price on the grid regarding the total NPC and COE for the microgrid system. Analysis shows that a lower sell-back price results in a higher total NPC and a higher cost of energy. In this study, the electricity sell-back price to the grid was assumed to be $0.08 per

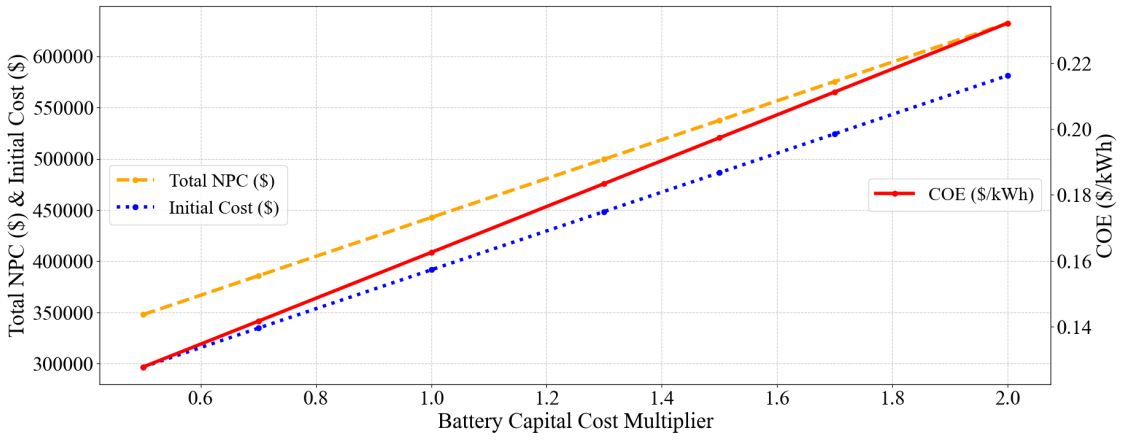

(a)

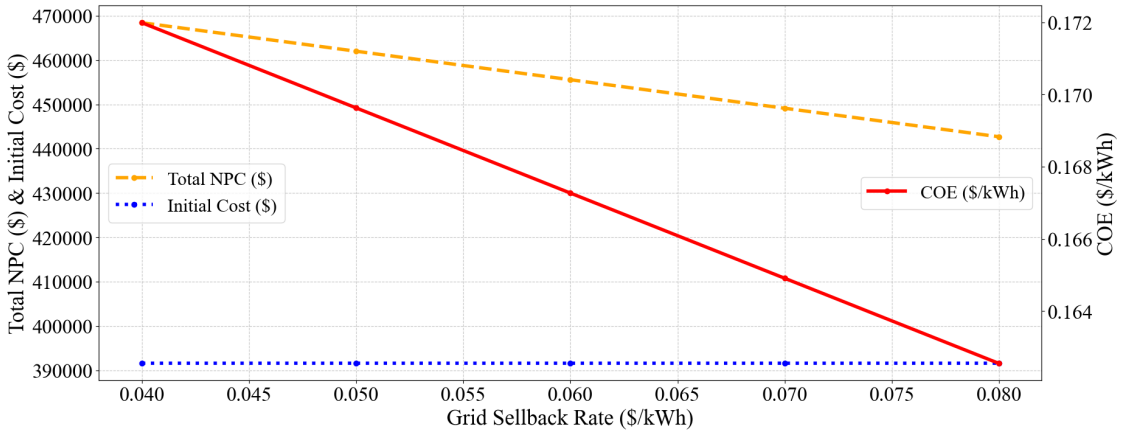

(b)

Figure 15: Key economic indicators due to fluctuations in battery and grid sell-back prices (a) battery capital cost, (b) electricity sell-back price to the grid.

kWh, yielding a total NPC of $442,700.50 and a COE of $0.1626 per kWh. However, if the sell-back price drops to $0.04 per kWh, the total NPC increases to $468,397 and the COE rises to $0.1720 per kWh. This increase is due to reduced revenue from electricity sales to the grid when the sell-back price decreases. Notably, the initial cost of the microgrid system remains unchanged despite these variations in grid electricity sell-back prices.

Overall fluctuations in capital costs of PV, WTG, and battery can significantly impact the microgrid's economic feasibility. The initial cost required for these components directly influences both investment decisions and long-term cost projections and may significantly alter the expected return on investment. Accordingly, accurate forecasting of these costs and their potential variability is essential for ensuring the successful implementation and operation of microgrid systems.

3.2. Operation Results and Discussion

In this section, the resilience operation of the proposed MILP-MPC microgrid is evaluated by comparing its performance with HOMER Pro results. Following this initial assessment, extensive scenarios are run to further examine its performance. The results of all these scenarios can be seen in Table 5.

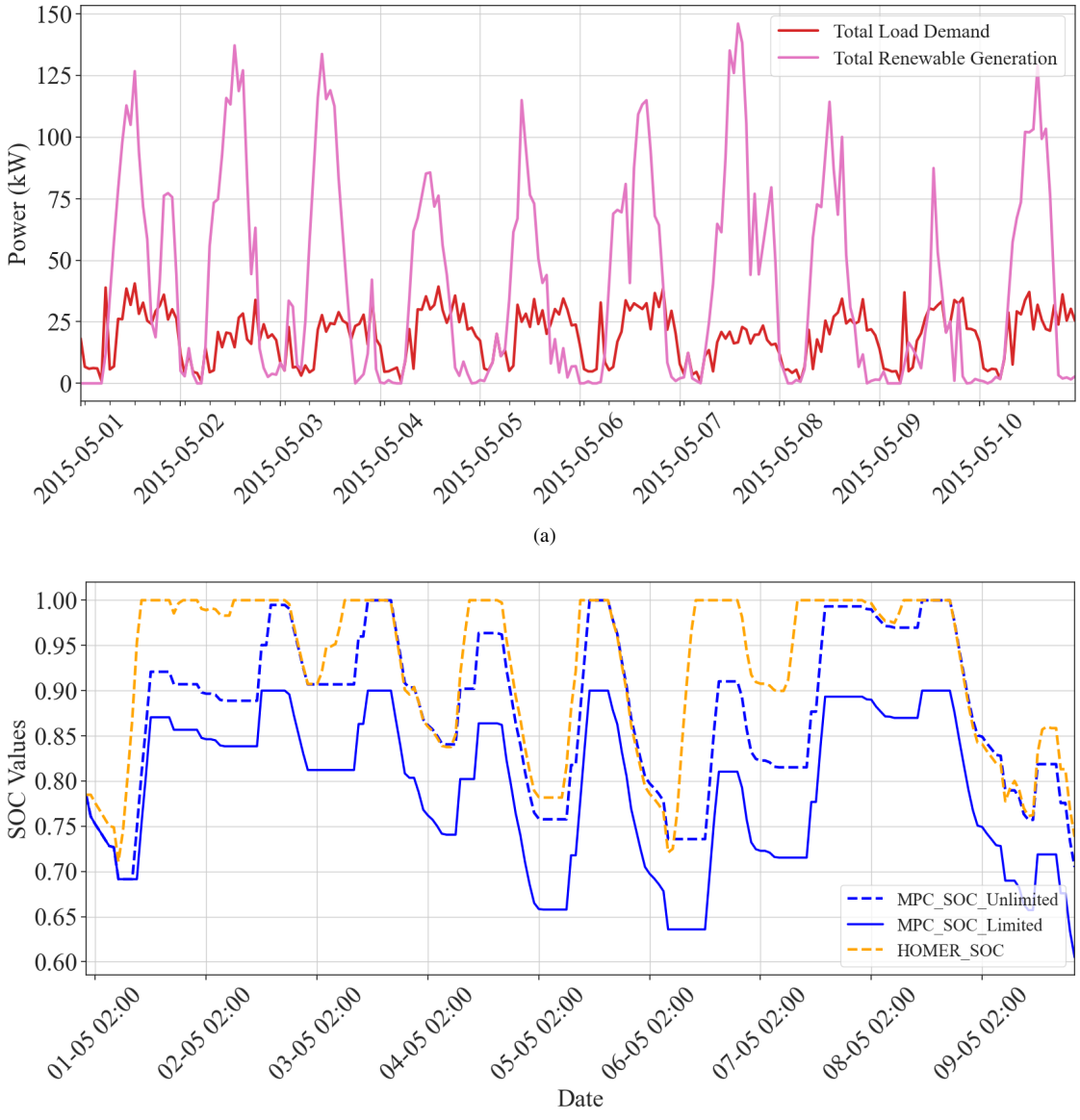

Figure 16: Validation of the proposed resilient operational method through comparison with HOMER Pro over a 10-day horizon (May 1–10): (a) total load and generation,(b) battery SOC results.

To benchmark the proposed MILP–MPC approach against an established microgrid software tool, the battery SOC profile over a 10-day horizon (May 1–10) is compared with results from HOMER Pro, which employs average daily data and treats each day independently. Figure 16a demonstrates the total renewable generation and load during this

period. Figure 16b illustrates three SOC trajectories: the first (MPC_SOC_Limited) represents the MILP–MPC model with an upper SOC boundary of 90%; the second (MPC_SOC_Unlimited) follows the same approach but allows the battery to charge up to 100%; and the third (HOMER_SOC) corresponds to the default HOMER Pro solution, which also permits a 100% SOC.

All three results serve the loads fully, but the trajectories reveal key operational differences. HOMER Pro often charges the battery rapidly whenever surplus generation appears, as it has no mechanism to anticipate future events. In contrast, the MILP–MPC framework "looks ahead" within its prediction horizon and chooses to idle the battery at certain times, thereby avoiding unnecessary charge–discharge cycles. For instance, near Day 3, HOMER Pro charges the battery aggressively up to 100% as soon as surplus energy becomes available. In contrast, the MILP–MPC approach moderates charging to better align with upcoming demand, maintaining the battery at a level that balances near-term generation with forecasted usage. Even with the 90% cap, the MILP–MPC model meets all loads, highlighting the robustness of a predictive optimization strategy. Moreover, limiting the SOC between 20% and 90% during normal operation plays a crucial role in enhancing battery longevity by reducing exposure to low or high charge levels, which can accelerate battery degradation over time. Although linearization introduces a minor approximation error (below 5%), it allows the problem to remain computationally feasible while achieving near-optimal solutions. Furthermore, while the linearized model is used in optimization, the final battery life expectancy is computed using a nonlinear formulation, ensuring that the results align with realistic degradation patterns.

Building on the validation part, the first 15 scenarios were run to determine the optimal weighting configuration for the objective function. It is also important to mention that in these 15 scenarios, essential and business loads do not participate in the demand response program, while deferred loads, as the name implies, completely participate in the demand response program with an allowance for a 100% shift in their demand. In Scenario 16, it is assumed that essential and business loads can slightly participate in the demand response program. Scenario 17 utilizes the smart resilience control proposed in Figure 9. Scenarios 18 to 24 investigate the impact of reduced battery capacity compared to the designed value, while utilizing the smart resilience controller. Scenarios 25 to 28 explore the possibility of connecting the microgrid to the main grid. It is assumed that the microgrid can import electricity as needed during grid-connected mode to mitigate deep discharges and prolong battery life during Stage 2 analyses. In Scenarios 25 and 26, the full capacity of the designed battery is used in the planning stage, while in Scenarios 27 and 28, only 25% of the designed capacity is utilized. Additionally, the potential profit from selling excess energy to the grid is examined in these four scenarios. In the following, scenarios outputs are described in detail.

Scenarios 2 to 5 focus on individual components of the objective function. In scenario 2, only the resiliency part is considered. Compared to scenarios 3 to 5, this results in less power loss and a good resiliency index over the 9

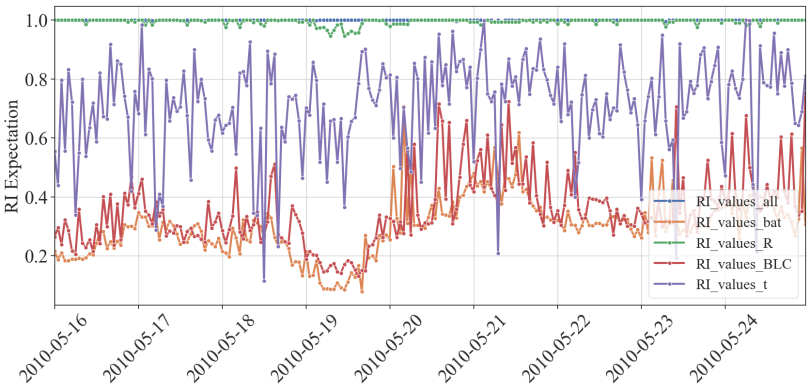

Figure 17: Expected Resiliency Index (RI) under different weighting schemes.

days of the HILP event. However, the conditions in switching are the worst among all scenarios. Scenario 3 focuses solely on the switching cost. The best answer in this case is no switching, which leads to a catastrophic resiliency index with many loads not being supplied. Despite this, the expected battery lifetime is 137.63 years, a result of the simulation indicating that no battery life is lost due to discharging. Scenario 4 considers only the BLC part. Since it relates to discharges, it is unsurprising that the battery is not used at all, resulting in an infinite battery life according to the formula. However, this scenario has the worst resiliency index compared to all others. In scenario 5, only the power balance equation is considered. This scenario achieves a better resiliency index compared to the previous ones but still falls short because it primarily addresses power imbalances and is not designed to enhance system resilience. It also results in the most battery discharges, similar to scenario 9, due to its focus on minimizing both positive and negative imbalances, which leads to unnecessary charging and discharging of the battery.

Moreover, the Expected Resiliency Index (ERI) curve, introduced by the authors as a novel resiliency metric, is illustrated for scenarios 2 to 5 in Figure 17. This curve represents the system's expected RI over the subsequent 24-hour period, calculated based on the decisions made within the MPC framework. At each point on the curve, the ERI reflects the anticipated resiliency, which is reassessed as the system transitions into each new 24-hour cycle. Consequently, this continuous evaluation generates a comprehensive visualization of the ERI throughout the specified time frame, without implying that the overall system resiliency reaches its minimum level. Scenarios 6 to 11 explore combinations of two objectives at a time. Scenario 9, which considers only resiliency and power imbalance, shows the best result in terms of supplying almost all loads. However, the number of discharges and total switches is the worst because the battery objectives are not accounted in the objective function. The expected battery lifetime in this scenario is 9.66 years, which is less favourable compared to other scenarios. It is worth mentioning that in scenario 11, which considers only BLC and resiliency, the best-expected battery lifetime is achieved. This scenario also performs better in terms of resiliency compared to all other scenarios except scenario 9. Additionally, the number of discharges is the second best among scenarios 6 to 11.

Scenarios 12 to 15 examine combinations of three out of the four objectives. In scenario 13, which considers BLC, total imbalance, and resiliency, a decent result is achieved in terms of load supply and resiliency index. However, this scenario still results in a high number of discharges and switches. Scenario 14, which replaces the BLC objective with the switching objective from scenario 13, yields the second-best result in terms of resiliency. In this scenario, the expected battery lifetime, total switches, and discharges are improved compared to scenario 13.

The best scenario is the first one, where all parts of the objective function are considered equally. This yields logical results with only about one-third of the business load lost and an almost perfect resiliency index of 1. The expected battery lifetime in this worst-case situation is 14.42 years, which indicates that even with potentially more charging and discharging, the expected lifetime remains close to the planning design of 15 years. Among scenarios with a resiliency index greater than 0.99, such as scenarios 2, 9, and 13, this scenario has the fewest switches and discharges. For visual comparison, Figure 18 illustrates battery SOC in scenarios 1 and 9. In Figure 18a, it is clear that the battery life is not prioritized, as the system charges and discharges almost every hour, with very few idle periods. However, in Figure 18b, the MPC demonstrates conservative battery usage, avoiding constant charging and discharging.

Figure 19 shows the value of each objective function in scenario 1, which is appropriately normalized between 0 and 1. This demonstrates the effective normalization of the objective functions. Comparing this figure with Figure 18b, during periods when the battery is in idle mode, such as between days 21 and 22, the normalized BLC values are improved. In addition, the total imbalances for essential, business, and agricultural (deferred) loads in scenario 1 are shown in Figure 20. There are no imbalances in essential and deferred loads, while business loads exhibit negligible imbalances.

In scenario 16, it is assumed that essential and business loads can shift a maximum of 10% of their demand, which is reasonable for high-priority loads where further shifting is not feasible. In this scenario, essential and business loads are almost fully supplied. For all scenarios, deferred load is assumed to be fully shiftable. Additionally, the expected battery longevity increases from 14.42 years in scenario 1 to 15.58 years in scenario 16. Figure 21 shows the load patterns after applying 10% demand response to essential and business loads. This scenario demonstrates that even a small-scale DR implementation can contribute to enhanced resilience and extended battery life. Since these types of loads are inherently difficult to adjust in real-world applications, this scenario was designed to provide a practical perspective rather than assuming full participation in demand response programs. The results show that shifting even a limited portion of the load reduces peak discharges, thereby reducing battery stress and increasing the overall system's operational lifespan. This suggests that targeted DR strategies can improve microgrid resiliency without requiring large-scale behavioral changes from end users.

Table 5: Simulation Scenarios and Results.

Scenario	Weighting Factors	TS	Essential Loss	Business Loss	Deffered Loss	Total Loss	RI	EY	DIS number
1	$\omega_R = 0.25, \omega_t = 0.25, \omega_{\text{bat}} = 0.25, \omega_{\text{BLC}} = 0.25$	7	≃0	0.3978	≃0	0.3979	0.9999	14.425	97
2	$\omega_R = 1.0, \omega_t = 0.0, \omega_{\text{bat}} = 0.0, \omega_{\text{BLC}} = 0.0$	45	1.7218	30.566	13.2381	45.526	0.9948	10.810	102
3	$\omega_R = 0.0, \omega_t = 0.0, \omega_{\text{bat}} = 1.0, \omega_{\text{BLC}} = 0.0$	0	1323.0564	973.1779	369.1734	2567.4605	0.36759	137.63	15
4	$\omega_R = 0.0, \omega_t = 0.0, \omega_{\text{bat}} = 0.0, \omega_{\text{BLC}} = 1.0$	0	1177.5799	987.3639	402.5166	2665.4079	0.3106	∞	0
5	$\omega_R = 0.0, \omega_t = 1.0, \omega_{\text{bat}} = 0.0, \omega_{\text{BLC}} = 0.0$	21	344.4674	642.2060	167.8735	1154.5471	0.7699	9.6637	120
6	$\omega_R = 0.0, \omega_t = 0.5, \omega_{\text{bat}} = 0.5, \omega_{\text{BLC}} = 0.0$	10	1045.7357	690.1659	90.2695	1826.1712	0.4765	32.0781	20
7	$\omega_R = 0.5, \omega_t = 0.0, \omega_{\text{bat}} = 0.5, \omega_{\text{BLC}} = 0.0$	0	487.5285	367.4426	145.1345	1000.1058	0.7443	∞	0
8	$\omega_R = 0.0, \omega_t = 0.0, \omega_{\text{bat}} = 0.5, \omega_{\text{BLC}} = 0.5$	0	1311.9293	774.7107	405.9348	2492.5748	0.33671	82.5825	25
9	$\omega_R = 0.5, \omega_t = 0.5, \omega_{\text{bat}} = 0.0, \omega_{\text{BLC}} = 0.0$	24	≃0	≃0	0.0003	0.000415	0.9999	9.6665	120
10	$\omega_R = 0.0, \omega_t = 0.5, \omega_{\text{bat}} = 0.0, \omega_{\text{BLC}} = 0.5$	22	721.116	910.9397	128.3236	1760.3795	0.5832	13.368	105
11	$\omega_R = 0.5, \omega_t = 0.0, \omega_{\text{bat}} = 0.0, \omega_{\text{BLC}} = 0.5$	0	353.0940	320.5975	183.061	856.7527	0.8037	89.3644	17
12	$\omega_R = 0.33, \omega_t = 0.0, \omega_{\text{bat}} = 0.33, \omega_{\text{BLC}} = 0.33$	0	318.0040	321.1475	204.5931	843.7447	0.81701	85.5490	20
13	$\omega_R = 0.33, \omega_t = 0.33, \omega_{\text{bat}} = 0.0, \omega_{\text{BLC}} = 0.33$	22	≃0	0.1010	0.5966	0.6977	0.9999	13.3286	106
14	$\omega_R = 0.33, \omega_t = 0.33, \omega_{\text{bat}} = 0.33, \omega_{\text{BLC}} = 0.0$	11	295.2484	195.3237	50.9615	541.5337	0.85063	30.7044	21
15	$\omega_R = 0.0, \omega_t = 0.33, \omega_{\text{bat}} = 0.33, \omega_{\text{BLC}} = 0.33$	7	626.5864	685.5575	109.3016	1421.4456	0.6506	14.5358	98
16 (DR = 10%)	$\omega_R = 25, \omega_t = 0.25, \omega_{\text{bat}} = 0.25, \omega_{\text{BLC}} = 0.25$	8	0.0001	≃0	0.3305	0.3308	0.9999	15.5806	90
17 (Smart SOC)	$\omega_R = 25, \omega_t = 0.25, \omega_{\text{bat}} = 0.25, \omega_{\text{BLC}} = 0.25$	7	≃0	0.3978	0.0004	0.3983	0.9999	14.3965	98
18 (75%)	$\omega_R = 25, \omega_t = 0.25, \omega_{\text{bat}} = 0.25, \omega_{\text{BLC}} = 0.25$	6	0.0001	1.4404	7.3999	8.8405	0.9993	11.4466	102
19 (50%)	$\omega_R = 25, \omega_t = 0.25, \omega_{\text{bat}} = 0.25, \omega_{\text{BLC}} = 0.25$	6	24.4823	67.7473	12.8009	105.0305	0.9809	9.3103	96
20 (Soc-50%)	$\omega_R = 25, \omega_t = 0.25, \omega_{\text{bat}} = 0.25, \omega_{\text{BLC}} = 0.25$	6	21.6323	40.7023	115.3986	77.7333	0.9852	8.9895	98
21 (Soc-w-50%)	$\omega_R = 25, \omega_t = 0.25, \omega_{\text{bat}} = 0.25, \omega_{\text{BLC}} = 0.25$	8	17.7714	68.8945	18.0915	104.7576	0.9833	9.0702	96
22 (25%)	$\omega_R = 25, \omega_t = 0.25, \omega_{\text{bat}} = 0.25, \omega_{\text{BLC}} = 0.25$	6	87.8225	140.9595	36.2263	265.0084	0.9444	8.5126	71
23 (SOC-25%)	$\omega_R = 25, \omega_t = 0.25, \omega_{\text{bat}} = 0.25, \omega_{\text{BLC}} = 0.25$	6	60.9311	116.2264	28.4003	205.5578	0.9590	7.3121	82
24 (SOC-w-25%)	$\omega_R = 25, \omega_t = 0.25, \omega_{\text{bat}} = 0.25, \omega_{\text{BLC}} = 0.25$	9	35.5838	182.2255	38.5804	256.3898	0.9611	7.4870	81
25 (Grid)	$\omega_R = 0.25, \omega_t = 0.25, \omega_{\text{bat}} = 0.25, \omega_{\text{BLC}} = 0.25$	0	≃0	≃0	≃0	≃0	≃1	≃∞	7
26 (Grid-Profit)	$\omega_R = 0.25, \omega_t = 0.25, \omega_{\text{bat}} = 0.25, \omega_{\text{BLC}} = 0.25$	10	≃0	≃0	≃0	≃0	≃1	27.07	58
27 (Grid-25%)	$\omega_R = 0.25, \omega_t = 0.25, \omega_{\text{bat}} = 0.25, \omega_{\text{BLC}} = 0.25$	0	≃0	≃0	≃0	≃0	≃1	≃∞	7
28 (Grid-Profit-25%)	$\omega_R = 0.25, \omega_t = 0.25, \omega_{\text{bat}} = 0.25, \omega_{\text{BLC}} = 0.25$	11	≃0	≃0	≃0	≃0	≃1	11.18	59

Note: ω_R: Resiliency Weighting Factor in Objective Function, ω_t: Total Imbalance Weighting Factor in Objective Function, ω_{bat}: Battery Switching Cost Weighting Factor in Objective Function, ω_{BLC}: Battery Life Cycle Weighting Factor in Objective Function, DR: Demand Response, TS: Total Switches, RI: Resilience Index, EY: Expected Years.

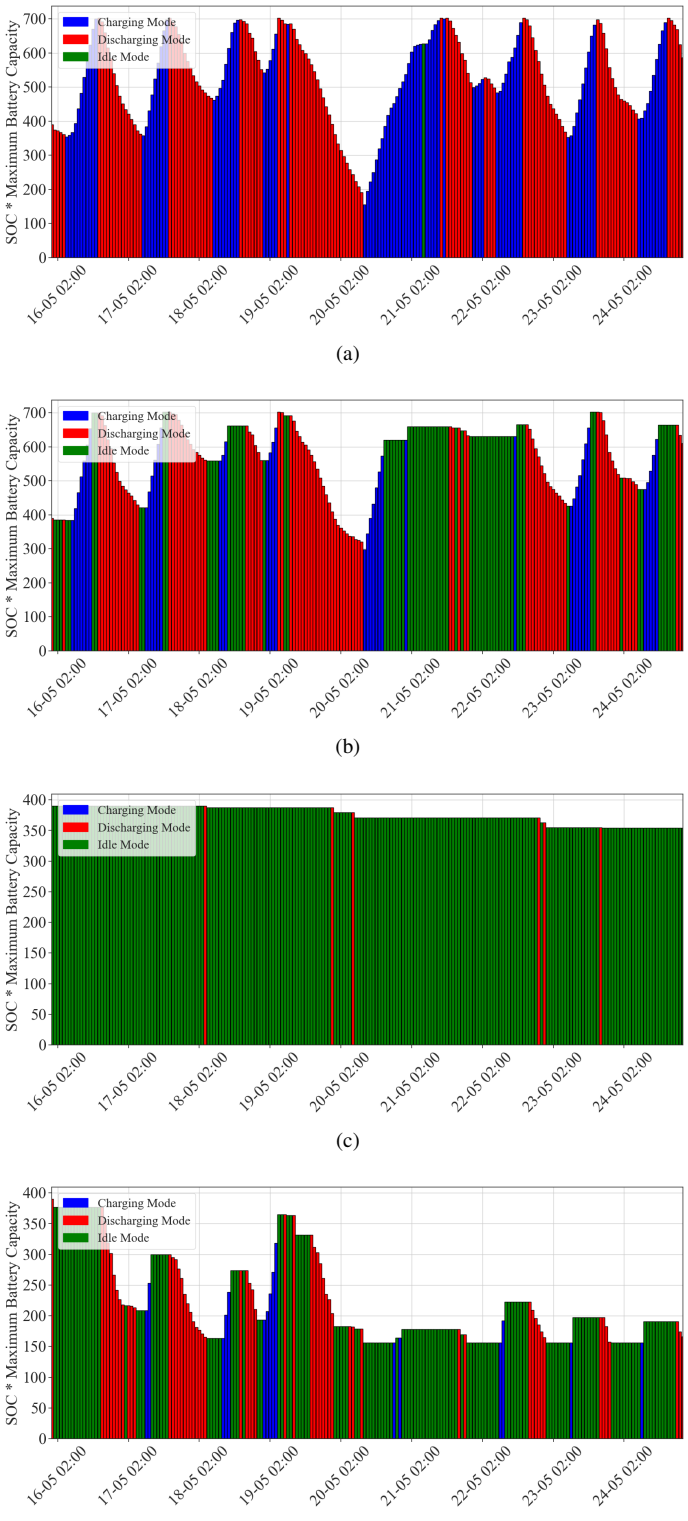

Figure 18: State of charge under different optimization objectives: (a) Considering only resiliency and total imbalance, (b) Considering all objectives, (c) Including the grid without profit, (d) Including the grid with profit.

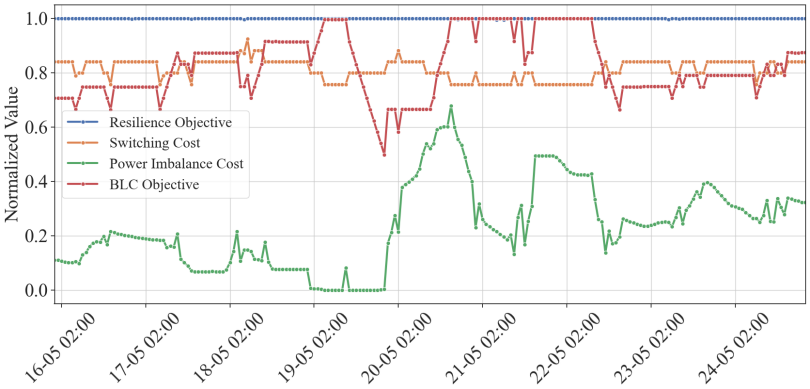

Figure 19: Different Objectives Normalized Values.

In scenario 17, the smart resilient control shown in Figure 9 was utilized. Given the adequate planned sizing of the microgrid, the results are similar to those in scenario 1, as the resiliency index rarely drops below 0.95. To demonstrate the performance of this control strategy, scenarios 18 to 24 were introduced with reduced battery capacity. These scenarios involve 75%, 50%, and 25% of the designed battery capacity from the planning phase.

Scenario 18 corresponds to 75% of the designed battery capacity. The smart controller yields similar results since the ERI still does not drop below 0.95. In this scenario, essential loads are fully met, and there is only 1.44 kW of business load loss, which is acceptable during a HILP event. However, the expected battery lifespan decreases to 11.44 years, 3 years less than in scenario 1. It is important to note that this expected lifespan pertains to operation during the HILP event; the battery may have greater longevity during normal operations. Therefore, from an operational perspective, maintaining 75% of the designed battery capacity still provides robust resiliency to HILP events.

In scenarios 19 to 21, half of the battery capacity is assumed. With this reduced capacity, the ERI drops below 95%, necessitating a detailed study across three scenarios. In scenario 19, the smart controller is not applied. Scenario 20 relaxes the SOC limits when the ERI falls below 0.95. Scenario 21 follows the approach of scenario 20 but further prioritizes the resiliency objective by setting it as the primary focus while de-emphasizing the other objectives. Scenario 21 results in less essential load loss compared to the other two scenarios, which aligns with the primary objective of using such a controller. Scenarios 20 and 21 show an improvement in the resiliency index compared to scenario 19. However, the high level of DOD reduces the expected battery lifespan to 9 years, which is 5.4 years less than the first scenario. Even with this battery sizing, only about 100 kW, or 2.41% of the total load, is lost during the HILP event. It is worth mentioning that the load loss occurs only on days 19 and 20 when generation is almost nonexistent.

In scenarios 22 to 24, one-fourth of the battery capacity is assumed. Here, the effect of the smart controller is more pronounced due to the substantial loss. Without the smart controller, 87.82 kW of essential load is lost. In contrast, with the full use of the smart controller in scenario 24, the loss is reduced to nearly one-third (35.58 kW)

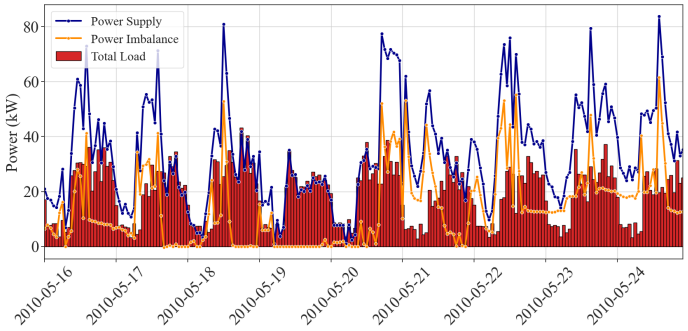

(a)

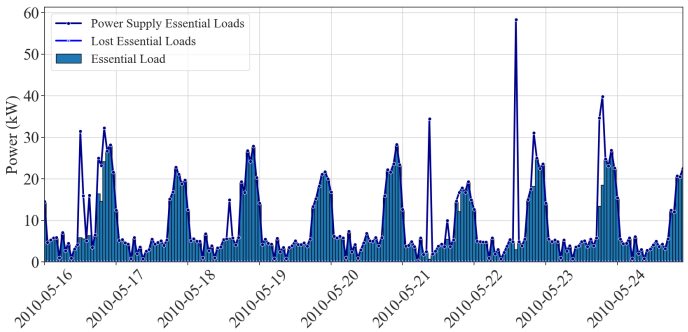

(b)

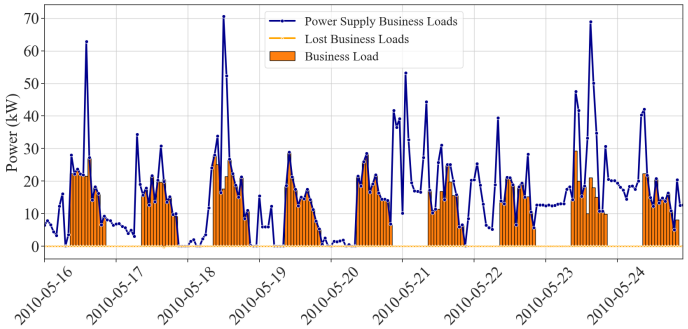

(c)

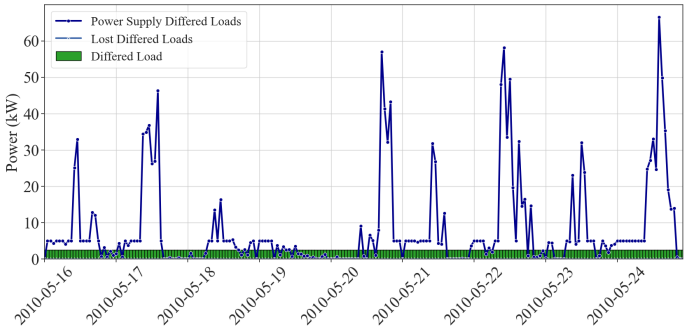

(d)

Figure 20: Load imbalance across different types of demands. (a) Total load imbalance, (b) Essential load imbalance, (c) Business load imbalance, (d) Deferrable load imbalance

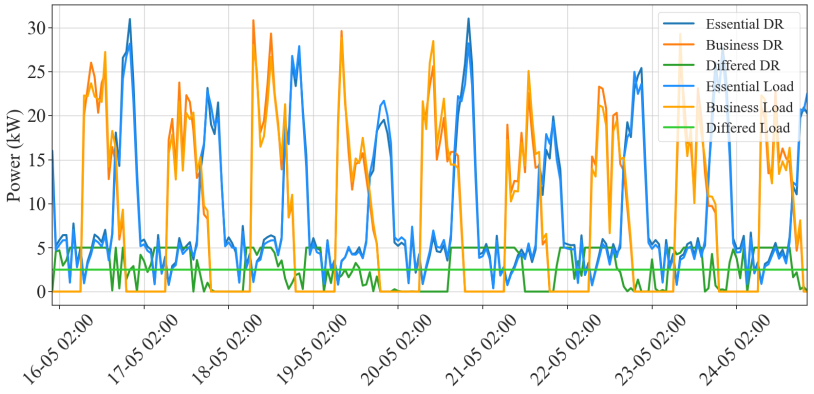

Figure 21: Essential and business load patterns after 10% demand response.

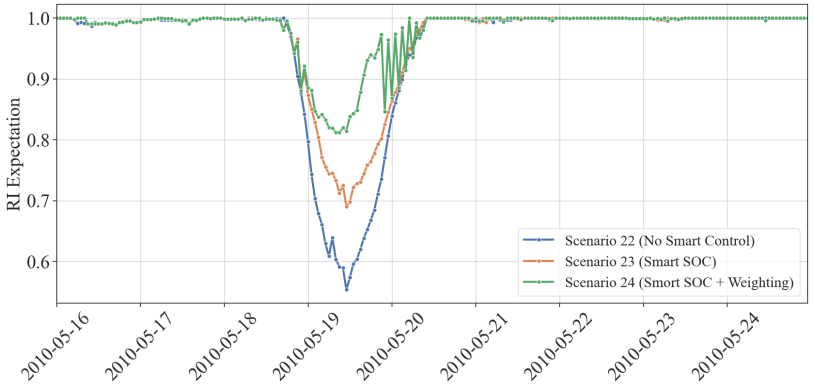

Figure 22: Effect of using smart resilient control on ERI when the battery capacity is 25% of the designed capacity.

for essential loads. Overall, the resiliency for 9 days remains at a commendable 0.96. However, due to the increased DOD, the battery life cycle drops to approximately 7.5 years, which is almost half of what it would be with a full capacity battery. The total loss in these scenarios amounts to about 250 kW, which translates to a 6% loss of the total load during these 9 days. To illustrate the benefits of these smart controls, Figure 22 compares the expected resiliency in scenarios 22 to 24. This Figure indicates that when smart resilience control is fully applied, the area under the curve decreases. It is important to note that the reduced battery life expectancy in scenarios with halved or quartered capacity is not solely due to the DOD needed for the HILP event. Rather, the high DOD primarily results from the decreased available capacity, which places greater demand on the battery and reduces its lifespan.

Scenarios 25 and 26 explore the effects of connecting the microgrid to the main grid, assuming continuous grid connection during the HILP event. Scenario 25 operates under the assumption of unrestricted electricity trade with the grid, without specific pricing for imports or exports, while Scenario 26 aims to maximize profit from electricity sales and minimize purchase costs. As indicated in Table 5, both scenarios maintain nearly full load coverage, achieving a resilience index of 1. Additionally, battery life is notably extended, by approximately 13 years in Scenario 26, compared to Scenario 1, where the microgrid operates in isolated mode. In Scenario 25, 900.82 kWh of electricity is

purchased, and 2,208.46 kWh of renewable generation is sold back to the grid. With an assumed selling price of 15 pence per kWh and a buying cost of 25 pence per kWh, the total profit over 9 days amounts to $106.06. Scenario 26 incorporates profit maximization as an additional objective, leading to reduced electricity purchases (240.97 kWh) and sales (2,010.27 kWh), while achieving a profit of $250.29, more than double that of Scenario 25, representing a 136% increase. The grid connection in both scenarios significantly reduces demand response mismatches towards the end of the period. Figures 18c and 18d depict the SOC for scenarios 25 and 26, respectively, while Figure 23 illustrates the buying and selling patterns. In Scenario 26, the optimization strategy prioritizes maximizing the benefit from the initial SOC for increased profit and only purchases electricity during the HILP event. In contrast, Scenario 25's optimization focuses on prolonging the battery life cycle by discharging in small increments rather than entering idle mode. In isolated mode, the microgrid continues to operate and supply critical loads, ensuring resilience even during extreme events like cyclones. However, when connected to the grid, the microgrid benefits from reduced dependency on local storage, as it can import off-peak electricity and sell surplus renewable energy. This reduces deep discharge cycles, improving battery lifespan and decreasing operational costs. Conversely, in a fully isolated configuration, the battery must handle all demand fluctuations, which can accelerate degradation. Scenarios 25 and 26 highlight these advantages, where the grid connection not only reduces stress on the battery but also enhances the overall system's cost efficiency. The ability to import cheaper electricity and sell excess power helps optimize both energy usage and storage performance. These findings highlight a trade-off between grid independence and local storage sustainability: being islanded ensures autonomy but may shorten battery life, whereas leveraging grid support preserves storage health.

In scenarios 27 and 28, the microgrid is connected to the main grid, but the battery capacity is reduced to one-fourth of its design specification. Despite this reduction, there is no loss of load, and the resilience index remains at 1. Additionally, the battery life extends by nearly three years compared to scenarios 22 to 24. In scenario 27, where the grid connection is added without considering profit, 891.03 kWh was purchased from the grid, while 2,210.85 kWh was sold back. This resulted in a cost of $222.75 for the purchased electricity and a revenue of $331.62 from the electricity sold, leading to a net benefit of $108.87. However, when profit is considered in the objective function in scenario 28, the microgrid purchased 211.31 kWh from the grid for $52.82 and sold 1,950.16 kWh, resulting in $292.52 revenue. This resulted in a net benefit of $239.69 during the HILP event, nearly 2 times greater than in scenario 27. The electricity import and export patterns for scenarios 27 and 28 are illustrated in Figure 23c and 23d, respectively.

4. Conclusion

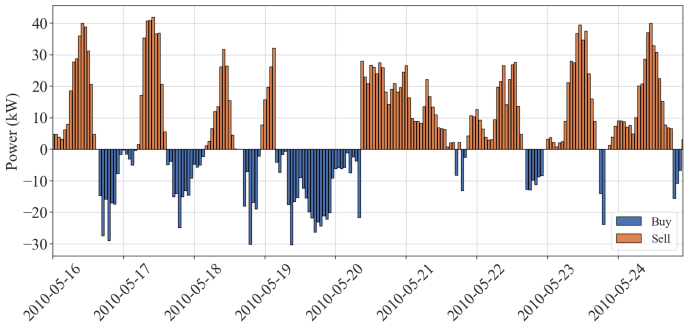

(a)

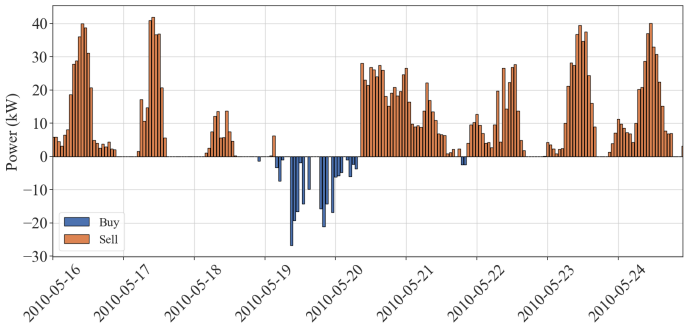

(b)

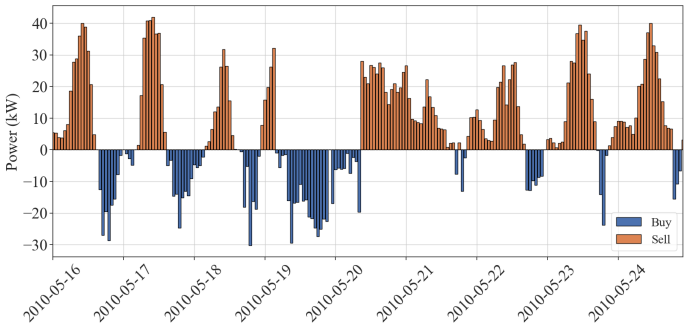

(c)

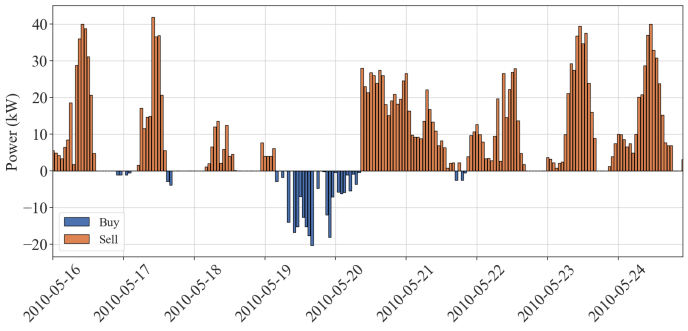

(d)

Figure 23: Electricity import and export from/to the grid: (a) Scenario 25 (b) Scenario 26, (c) Scenario 27, (d) Scenario 28.

The study aimed to develop a comprehensive two-stage framework for resilient microgrid planning and operation in cyclone-prone regions. By integrating realistic design, battery longevity, and proactive resiliency strategies, the framework sought to enhance the reliability and sustainability of energy systems in vulnerable areas. This approach combines location-specific sizing, validated operational performance under High-Impact Low-Probability (HILP) events, and explicit modeling of battery degradation and demand response mechanisms.

Findings demonstrated the effectiveness of this framework through a case study in a coastal village in Andhra Pradesh, India. A 140-kW PV, 80-kW wind turbine, and 780-kWh lithium-ion battery system, designed using HOMER Pro, showcased robust performance. The system achieved a Cost of Energy of 0.163/kWh in grid-connected mode, compared to 0.237/kWh in islanded mode, while successfully meeting load demand during Cyclone Laila. A key innovation was the use of a Mixed-Integer Linear Programming powered Model Predictive Control strategy, which incorporated a piecewise linear Battery Life Cycle–Depth of Discharge model. This reduced computational complexity and extended battery life to 15.5 years. Including Expected Resiliency Index and power imbalance in the optimization ensured a 99.99% load supply during the cyclone, even with reduced battery capacity. For instance, maintaining just 25% of the battery capacity still achieved a resiliency index of 0.96. Sensitivity analyses further confirmed the system's viability under cost fluctuations, with grid connectivity doubling battery life through reduced discharge cycles and enabling profit from surplus energy sales.

The implications of these findings are significant. The framework offers a scalable solution for regions vulnerable to extreme weather, balancing autonomy and sustainability. The approach reduces operational costs and capital expenditures over the system lifecycle by prioritizing battery longevity and resiliency. The 10% DR participation for essential and business loads highlights practical pathways to enhance resilience without requiring major behavioral shifts. Additionally, grid connectivity provides a trade-off between battery preservation and energy independence.

However, the study focused on a single HILP event (Cyclone Laila) and assumed full DR participation for deferred loads. Future research will also extend this framework to multi-microgrid networks with energy-sharing protocols, aiming to enhance the resilience and efficiency of energy systems in diverse and challenging environments.

References

[1] M. H. N. Amiri and F. Guéniat, "Towards a framework for measurements of power systems resiliency: Comprehensive review and development of graph and vector-based resilience metrics," Sustainable Cities and Society, p. 105517, 2024.

[2] M. H. Nejati Amiri, M. Mehdinejad, A. Mohammadpour Shotorbani, and H. Shayanfar, "Heuristic retailer's day-ahead pricing based on online-learning of prosumer's optimal energy management model," Energies, vol. 16, no. 3, p. 1182, 2023.

[3] H. Masrur, H. Khaloie, A. T. Al-Awami, S. El Ferik, and T. Senjyu, "Cost-aware modeling and operation of interconnected multi-energy microgrids considering environmental and resilience impact," Applied Energy, vol. 356, p. 122320, 2024.

[4] M. Yin, K. Li, and J. Yu, "A data-driven approach for microgrid distributed generation planning under uncertainties," Applied Energy, vol. 309, p. 118429, 2022.

[5] M. S. Abid, H. J. Apon, S. Hossain, A. Ahmed, R. Ahshan, and M. H. Lipu, "A novel multi-objective optimization based multi-agent deep reinforcement learning approach for microgrid resources planning," Applied Energy, vol. 353, p. 122029, 2024.

[6] M. Borghei and M. Ghassemi, "Optimal planning of microgrids for resilient distribution networks," International Journal of Electrical Power & Energy Systems, vol. 128, p. 106682, 2021.

[7] N. N. Ibrahim, J. J. Jamian, and M. M. Rasid, "Optimal multi-objective sizing of renewable energy sources and battery energy storage systems for formation of a multi-microgrid system considering diverse load patterns," Energy, vol. 304, p. 131921, 2024.

[8] K. Pang, J. Zhou, S. Tsianikas, D. W. Coit, and Y. Ma, "Long-term microgrid expansion planning with resilience and environmental benefits using deep reinforcement learning," Renewable and Sustainable Energy Reviews, vol. 191, p. 114068, 2024.

[9] P. Kurukuri, M. R. Mohamed, P. H. Raavi, and Y. Arya, "Optimal planning and designing of microgrid systems with hybrid renewable energy technologies for sustainable environment in cities," Environmental Science and Pollution Research, pp. 1–18, 2024.

[10] M. M. Kamal, I. Ashraf, and E. Fernandez, "Planning and optimization of microgrid for rural electrification with integration of renewable energy resources," Journal of Energy Storage, vol. 52, p. 104782, 2022.

[11] E. G. Vera, C. A. Cañizares, M. Pirnia, T. P. Guedes, and J. D. M. Trujillo, "Two-stage stochastic optimization model for multi-microgrid planning," IEEE Transactions on Smart Grid, vol. 14, no. 3, pp. 1723–1735, 2022.

[12] S. Phommixay, M. L. Doumbia, and Q. Cui, "A two-stage two-layer optimization approach for economic operation of a microgrid under a planned outage," Sustainable Cities and Society, vol. 66, p. 102675, 2021.

[13] S. Yang, J. Fang, Z. Zhang, S. Lv, H. Lin, and L. Ju, "Two-stage coordinated optimal dispatching model and benefit allocation strategy for rural new energy microgrid," Energy, vol. 292, p. 130274, 2024.

[14] F. Amini, S. Ghassemzadeh, N. Rostami, and V. S. Tabar, "A stochastic two-stage microgrid formation strategy for enhancing distribution network resilience against earthquake event incorporating distributed energy resources, parking lots and responsive loads," Sustainable Cities and Society, vol. 101, p. 105191, 2024.

[15] Y. Wang, A. O. Rousis, and G. Strbac, "A three-level planning model for optimal sizing of networked microgrids considering a trade-off between resilience and cost," IEEE Transactions on Power Systems, vol. 36, no. 6, pp. 5657–5669, 2021.

[16] M. Ghasemi, A. Kazemi, A. Mazza, and E. Bompard, "A three-stage stochastic planning model for enhancing the resilience of distribution systems with microgrid formation strategy," IET Generation, Transmission & Distribution, vol. 15, no. 13, pp. 1908–1921, 2021.

[17] V. S. Saravi, M. Kalantar, and A. Anvari-Moghaddam, "A cooperative resilience-oriented planning framework for integrated distribution energy systems and multi-carrier energy microgrids considering energy trading," Sustainable Cities and Society, vol. 100, p. 105039, 2024.

[18] S. Mansouri, F. Zishan, O. D. Montoya, M. Azimizadeh, and D. A. Giral-Ramírez, "Using an intelligent method for microgrid generation and operation planning while considering load uncertainty," Results in Engineering, vol. 17, p. 100978, 2023.

[19] B. Dey, S. Misra, and F. P. G. Marquez, "Microgrid system energy management with demand response program for clean and economical operation," Applied Energy, vol. 334, p. 120717, 2023.

[20] Y. Liu, S. Yang, D. Li, and S. Zhang, "Improved whale optimization algorithm for solving microgrid operations planning problems," Symmetry, vol. 15, no. 1, p. 36, 2022.

[21] H. Khaloie, A. Abdollahi, M. Rashidinejad, and P. Siano, "Risk-based probabilistic-possibilistic self-scheduling considering high-impact low-probability events uncertainty," International Journal of Electrical Power & Energy Systems, vol. 110, pp. 598–612, 2019.

[22] M. Shehzad and F. Gueniat, "Modeling and optimal control of energy storage strategy for battery life extension via model predictive control," in 2021 European Control Conference (ECC), pp. 1981–1986, IEEE, 2021.

[23] M. H. N. Amiri, F. Annaz, M. De Oliveira, and F. Gueniat, "Strategies for resilience and battery life extension in the face of communication losses for isolated microgrids," in 2024 IEEE International Conference on Omni-layer Intelligent Systems (COINS), pp. 1–5, 2024.

[24] A. Nawaz, J. Wu, J. Ye, Y. Dong, and C. Long, "Distributed mpc-based energy scheduling for islanded multi-microgrid considering battery degradation and cyclic life deterioration," Applied energy, vol. 329, p. 120168, 2023.

[25] M. Amini, M. B. Sanjareh, M. H. Nazari, G. Gharehpetian, and S. H. Hosseinian, "A novel model for battery optimal sizing in microgrid planning considering battery capacity degradation process and thermal impact," IEEE Transactions on Sustainable Energy, 2024.

[26] A. Noutash and M. Kalantar, "Resilience enhancement with transportable storage systems and repair crews in coupled transportation and distribution networks," Sustainable Cities and Society, vol. 99, p. 104922, 2023.

[27] J. An and T. Hong, "Multi-objective optimization for optimal placement of shared battery energy storage systems in urban energy communities," Sustainable Cities and Society, p. 106178, 2025.

[28] R. Sarkar, P. K. Saha, S. Mondal, and A. Mondal, "Mage: Microgrids with advanced grid efficiency through battery-aware ev management," Sustainable Cities and Society, vol. 107, p. 105399, 2024.

[29] J. Rao, Y. He, and J. Liu, "Standalone versus grid-connected? operation mode and its economic and environmental assessment of railway transport microgrid," Sustainable Cities and Society, vol. 98, p. 104811, 2023.

[30] M. Amini, M. H. Nazari, and S. H. Hosseinian, "Optimal energy management of battery with high wind energy penetration: A comprehensive linear battery degradation cost model," Sustainable Cities and Society, vol. 93, p. 104492, 2023.

[31] S. A. Shezan, K. N. Hasan, A. Rahman, M. Datta, and U. Datta, "Selection of appropriate dispatch strategies for effective planning and operation of a microgrid," Energies, vol. 14, no. 21, p. 7217, 2021.

[32] H. U. R. Habib, A. Waqar, A. K. Junejo, M. F. Elmorshedy, S. Wang, M. S. Büker, K. T. Akindeji, J. Kang, and Y.-S. Kim, "Optimal planning and ems design of pv based standalone rural microgrids," IEEE Access, vol. 9, pp. 32908–32930, 2021.

[33] T. Huld, R. Müller, and A. Gambardella, "A new solar radiation database for estimating pv performance in europe and africa," Solar energy, vol. 86, no. 6, pp. 1803–1815, 2012.

[34] European Commission, Joint Research Centre, "Photovoltaic geographical information system (pvgis)," 2024. Accessed: 2024-09-03.

[35] C. Phurailatpam, B. S. Rajpurohit, and L. Wang, "Planning and optimization of autonomous dc microgrids for rural and urban applications in india," Renewable and Sustainable Energy Reviews, vol. 82, pp. 194–204, 2018.

[36] R. Sen and S. C. Bhattacharyya, "Off-grid electricity generation with renewable energy technologies in india: An application of homer," Renewable energy, vol. 62, pp. 388–398, 2014.

[37] B. K. Das, N. Hoque, S. Mandal, T. K. Pal, and M. A. Raihan, "A techno-economic feasibility of a stand-alone hybrid power generation for remote area application in bangladesh," Energy, vol. 134, pp. 775–788, 2017.

[38] S. Singh and S. C. Kaushik, "Optimal sizing of grid integrated hybrid pv-biomass energy system using artificial bee colony algorithm," IET Renewable Power Generation, vol. 10, no. 5, pp. 642–650, 2016.

[39] S. Singh, M. Singh, and S. C. Kaushik, "Feasibility study of an islanded microgrid in rural area consisting of pv, wind, biomass and battery energy storage system," Energy Conversion and Management, vol. 128, pp. 178–190, 2016.

[40] P. Malik, M. Awasthi, and S. Sinha, "A techno-economic investigation of grid integrated hybrid renewable energy systems," Sustainable Energy Technologies and Assessments, vol. 51, p. 101976, 2022.

[41] S. Dhundhara, Y. P. Verma, and A. Williams, "Techno-economic analysis of the lithium-ion and lead-acid battery in microgrid systems," Energy conversion and management, vol. 177, pp. 122–142, 2018.

[42] Waaree, "1kw on-grid solar system price in india," (2023), https://waaree.com/blog/1kw-on-grid-solar-system-price-in-india-2023/.

[43] S. C. Bhattacharyya, "Mini-grid based electrification in bangladesh: Technical configuration and business analysis," Renewable Energy,

vol. 75, pp. 745–761, 2015.

[44] E-vehicleinfo.com, "Lithium-ion battery prices in india from 1kwh to 10 kwh," 2023, https://e-vehicleinfo.com/lithium-ion-battery-prices-in-india/.

[45] S. Mahapatra and S. Dasappa, "Rural electrification: Optimising the choice between decentralised renewable energy sources and grid extension," Energy for sustainable development, vol. 16, no. 2, pp. 146–154, 2012.

[46] WindPowerLib_Developers, "Windpowerlib: A python library for wind power simulation and analysis," 2024. Accessed: 2024-09-03.

[47] K. S. Anderson, C. W. Hansen, W. F. Holmgren, A. R. Jensen, M. A. Mikofski, and A. Driesse, "pvlib python: 2023 project update," Journal of Open Source Software, vol. 8, no. 92, p. 5994, 2023.

[48] H. Qiu, W. Gu, Z. Wu, S. Zhou, G. Pan, X. Yang, X. Yuan, and X. Ding, "Resilience-directional robust power dispatching of microgrids under meteorological disasters," IET Renewable Power Generation, vol. 13, no. 12, pp. 2084–2093, 2019.